



## RESEARCH ARTICLE

10.1029/2020MS002402

## Key Points:

- A conceptual model for convective density currents is proposed: a cold pool adjacent to at least one gust front
- A new method is designed to identify such structures in high-resolution simulations
- Density currents' thermodynamical, dynamical, and morphological properties are derived

## Correspondence to:





N. Rochetin,  
[nicolas.rochetin@lmd.ipsl.fr](mailto:nicolas.rochetin@lmd.ipsl.fr)

## Citation:

Rochetin, N., Hohenegger, C., Touzé-Peiffer, L., & Villefranque, N. (2021). A physically based definition of convectively generated density currents: Detection and characterization in convection-permitting simulations. *Journal of Advances in Modeling Earth Systems*, 13, e2020MS002402. <https://doi.org/10.1029/2020MS002402>

Received 6 NOV 2020  
Accepted 6 JUN 2021

# A Physically Based Definition of Convectively Generated Density Currents: Detection and Characterization in Convection-Permitting Simulations

Nicolas Rochetin<sup>1,2</sup> , Cathy Hohenegger<sup>1</sup> , Ludovic Touzé-Peiffer<sup>3</sup> , and Najda Villefranque<sup>4</sup> 

<sup>1</sup>Max-Planck-Institut für Meteorologie (MPI), Hamburg, Germany, <sup>2</sup>Laboratoire de Météorologie Dynamique (LMD), Ecole Normale Supérieure (ENS), Paris, France, <sup>3</sup>Laboratoire de Météorologie Dynamique (LMD), Sorbonne University, Paris, France, <sup>4</sup>Centre National de Recherches Météorologiques (CNRM), Météo France, Toulouse, France

**Abstract** In this study, a conceptual model to define convective density currents is proposed. Based on theory, observations and modeling studies, we define convective density currents as 3D coherent structures with an anomalously cold core, an adjacent wind gust, and a vertical structure made of two layers: a well-mixed one near the surface and a stratified one above. With this definition, a methodology is proposed to identify and label individual convective density currents in convection-permitting simulations. The method is applied to four distinct cloud scenes taken from a convection-permitting simulation. Our methodology reveals new dynamic, thermodynamic, and geometric features related to the density currents' imprint on the planetary boundary layer. The method is found to be (i) relevant in distinct convective regimes, (ii) relevant in land and oceanic situations, and (iii) adapted to both Cloud Resolving Models and Large Eddy Simulations. It also provides proxies such as the number, the spatial coverage, the mean radius, and the mean velocity of convective density currents, from which a detailed analysis of their role in the life-cycle and spatial organization of convection could be performed in the near future.

**Plain Language Summary** Convective density currents are dense flows generated at the vicinity of storms, which form, thanks to the evaporation of rain droplets in the clear air surrounding the clouds and below them. Evaporation induces a cooling of the air. Cooled air becomes denser than its surrounding, it sinks and spreads at the surface. Since these flows induce a significant cooling at the surface, convectively generated density currents are commonly referred to as “cold pools” in the community. Based on this consideration, we designed a method to specifically detect and identify convective density currents as coherent three-dimensional structures in high-resolution numerical simulations of the atmosphere. The method is adapted to various meteorological situations and model types. We could also extract new diagnostics describing the collective behavior of convective density currents, potentially of great importance for the understanding of cloud and precipitation dynamics.

## 1. Introduction

Evaporation of precipitation or melting of solid hydrometeors contributes to the formation of cold negatively buoyant air inside a convective cloud, sometimes resulting in unsaturated downdrafts. This downdraft air sinks throughout the troposphere and spreads horizontally when it encounters the surface. Sometimes referred to as cold air mass (Charba, 1974), cold outflow (Rotunno et al., 1988) or cold pool (Black, 1978), the cold downdraft air spreading at the surface is now generally referred to by the generic term of cold pool. Cold pools from deep convection are in most cases characterized by a cold and dry core, surrounded by a ring of elevated moisture and high wind at their edge, the gust front. The propagation of cold pools in the warm ambient air is akin to the propagation of a dense fluid into a lighter fluid and cold pools can be viewed as a form of density current (Charba, 1974; Droegeemeier & Wilhelmson, 1987). Cold pools are not only an accompanying feature of deep convection, but they significantly affect the lifecycle of deep convection through their control on its organization (Rotunno et al., 1988; Wakimoto, 1982), their impacts on the transition from shallow to deep convection (Böing et al., 2012; M. F. Khairoutdinov & Randall, 2006), and on the triggering of new convective cells (Craig & Goff, 1976; Warner et al., 1980).

© 2021. LMD/CNRS/IPSL.

This is an open access article under the terms of the [Creative Commons Attribution-NonCommercial-NoDerivs](https://creativecommons.org/licenses/by-nc-nd/4.0/) License, which permits use and distribution in any medium, provided the original work is properly cited, the use is non-commercial and no modifications or adaptations are made.

In General Circulation Models (GCMs), one of the first attempts to parameterize density currents was proposed by Qian et al. (1998). Later on, Grandpeix and Lafore (2010) and Grandpeix et al. (2010) implemented a density current parameterization into the LMDZ GCM (i.e., the GCM developed at the “Laboratoire de Meteorologie Dynamique”—LMD). The inclusion of this process has now been clearly identified as key for convective memory (Colin et al., 2019) and for the representation of convective organization (Feng et al., 2015; Haerter, 2019; Jeevanjee & Romps, 2013; Seifert & Heus, 2013; Vogel et al., 2016). Other parameterizations of density currents coupled to deep convection have been proposed (Pantillon et al., 2015; Park, 2014). However, these parameterizations still rely on the knowledge of several parameters such as the spatial density of density currents, their spatial coverage, their velocity and their height, parameters which are poorly constrained from nonhydrostatic simulations and observations.

Given the importance of cold pools for the lifecycle of deep convection, cold pool characteristics have been scrutinized in observations and model simulations. This requires a detection method, and therefore a definition of cold pools. From the results of point measurements and selected case studies conducted over land, a cold pool passage can be recognized by a rapid and strong drop in temperature, an increase in pressure, the occurrence of strong winds and a change in wind direction (Craig & Goff, 1976; Engerer et al., 2008; McDonald & Weiss, 2021; Provod et al., 2016; Redl et al., 2015). Similar characteristics accompany cold pool passages over tropical ocean, albeit weaker (de Szoeke et al., 2017; Feng et al., 2015; Terai & Wood, 2013).

In recent observational studies, like that of Provod et al. (2016); de Szoeke et al. (2017); Zuidema et al. (2017), the detection of cold pool is actually closer to a density current-oriented detection, in which temperature, pressure, and wind variations are taken into consideration. In observations conducted during the DYNAMO (Gottschalck et al., 2013) campaign (de Szoeke et al., 2017; Zuidema et al., 2017) and at the Barbados Cloud Observatory—hereafter BCO—(Vogel et al., 2021), cold pools were detected in two phases: (i) first, a wind gust is recorded if a temperature drop exceeds a certain threshold  $\gamma$  such as  $(\partial T / \partial t)_{\text{gust}} \leq \gamma$ , where  $\gamma$  is usually close to  $-10^{-3} \text{ K s}^{-1}$ ; (ii) second, if the amplitude of the temperature perturbation on both sides of the gust exceeds a certain threshold  $\mu$  such as  $\Delta T_{\text{gust}} \leq \mu$  ( $\sim -0.5 \text{ K}$ ).

High-resolution model simulations are a useful complement to observations since they provide three-dimensional information on cold pools, which is not directly available from point measurements, but thought to be important for the understanding of the life cycle of deep convection (Schlemmer & Hohenegger, 2014). Due to the large amount of data that such simulations entail, several automated methods of cold pool detection have been proposed in the literature. In these methods, cold pools are defined as a set of connected points (an object) fulfilling some conditions; the latter generally based on an horizontal anomaly in buoyancy. Drager and van den Heever (2017) give an overview of the various measures that have been proposed to detect cold pools and of their strengths and weaknesses. They concluded that an algorithm based on surface rainfall rates and radial gradients in the density potential temperature field works best. The detection algorithm of Drager and van den Heever (2017) was tested for an idealized case. However, since cold pools can travel far away from the cloud they originate, they do not forcibly match surface precipitation patterns. Moreover, buoyancy anomalies can be initiated by a local cooling of the surface due to evapotranspiration after a rainfall event. Then, such a technique may hardly be transposable to more realistic situations. Other more complicated techniques, which combine atmospheric variables with Lagrangian particles to detect either cold pools (Torri et al., 2015; Torri & Kuang, 2016, 2019) or their associated gust front (Henneberg et al., 2020) have been proposed. The limitations of these latter techniques are that Lagrangian particles (i) have sometimes to be seeded (Henneberg et al., 2020) from a given level, but above all (ii) they must be followed in time.

The “cold pool” denomination has been extensively used in the past 10 years in the frame of idealized simulations over oceanic surfaces, among the ones cited above. Nevertheless, in pioneering studies, cold outflows, gust fronts or density currents, instead of cold pools, have been mostly analyzed, especially in the context of axisymmetric squall lines occurring over relatively dry lands or midlatitude summerlands using theoretic, observational or Cloud Resolving Model (CRM) simulations traveling storms, mesoscale convective systems (MCS) and squall-lines, using theoretical (M. Moncrieff, 1978; M. W. Moncrieff, 1992), experimental (Charba, 1974; Simpson, 1969), observational (Browning & Ludlam, 1962; Craig & Goff, 1976; Fankhauser, 1976; Wakimoto, 1982), or numerical (A. J. Thorpe & Miller, 1978; A. Thorpe et al., 1980; Dudhia et al., 1987) studies. In the first approach, cold pools are generally seen as circular patterns in the

Planetary Boundary Layer (PBL), which can be sustained for several hours depending on the ability of the PBL to recover (i.e., through surface fluxes). In the latter picture, density currents are embedded into a multicell system as one of the numerous building blocks constituting its internal dynamics. In explicit simulations, like Large Eddy Simulations (LES) or CRM, among the many recent studies devoted to cold pools tracking (Gentine et al., 2016; Torri et al., 2015; Torri & Kuang, 2019) or their associated gusts (Fournier & Haerter, 2019; Henneberg et al., 2020), none really considers these two components as a whole. Indeed, these studies only track cold pools (i.e., buoyancy anomaly) or the gust front (i.e., wind divergence), whereas we want to detect both features. From this perspective, one might use the word “convective density current” instead of “cold pool” to designate a divergent flow comprising a strong buoyancy discontinuity with its environment behind a gust front. This choice is motivated by the importance of characterizing the 3D structure of these flows, rather than just considering a 2D quasi-circular perturbation at the surface and just above it. From the perspective of fluid mechanics, the use of “density current” to designate these flows generated by convection solely might be confusing. Indeed, this term refers to the whole family of gravity-driven flows, including also breeze circulations. However, in this study, we will only focus on density currents associated to cold outflows, that is, convective density currents initiated near a rainshaft. But for simplicity, in the following we will refer to these convective density currents as density currents.

Assumptions concerning the density currents’ intrinsic properties and imprints on the near-environment are required to frame a coherent 3D structure emerging from the mean flow features (see Section 2). Starting from this conceptual picture, it is then possible to design a methodology to define density currents from absolute thermodynamical and dynamical fields, rather than anomalies. This choice allows:

1. To define density currents in a unique and rigorous way, so that their properties can be compared in various situations (e.g., land vs. ocean, day vs. night, shallow vs. deep convection or flat vs. complex topography), but without prescribing any horizontal scale of reference for the so-called “large-scale environment” (e.g., as for cold pool detection through anomalies with regard to a spatial average) and without any threshold in surface precipitation. This should reduce the sensitivity of the detection protocol to domain size and to meteorological situation.
2. To extract more information about the geometry and the statistics of density currents (e.g., height, radius, fractional coverage or spatial density).
3. To better understand their internal dynamics and their interactions with the large-scale flow (e.g., relative velocity, vorticity, divergence, vertical velocity along the gust, temperature, humidity or surface fluxes).
4. To open the way to a future Lagrangian tracking of density currents, in order to study the evolution of all these properties along their lifetime.

After proposing a general definition for density currents in Section 2, we test our detection algorithm using the output of a realistically configured convection-permitting simulation that was run over the tropical Atlantic (Klocke et al., 2017). The simulation and method are described in Section 3, the detection procedure is detailed in Section 4, the results are analyzed in Section 5 and conclusions are given in Section 6.

## 2. Conceptual Picture of Density Currents

Figure 1 displays a schematic illustrating that will be referred to as “density current” in the following. In this schematic, some of the displayed aspects are very well established (i.e., valid in shallow and deep regimes) and are labeled in *italic font*. Others, in **bold font**, are assumptions blending observational, experimental, theoretical, and numerical studies cited in the last section. This type of properties are divided in two further groups: a first group (in **bold black font**) for intrinsic properties of density currents, which will be used to design the detection method; and a second group (**bold gray font**) for additional properties they might exhibit. The whole study relies on these definition choices that are fully explained in this section.

### 2.1. A Spatially Coherent Structure

First, it can be safely stated that a density current is a 3D coherent structure, that is, a process distinct from its surrounding environment. Here, the divergent flow is generated at the vicinity of the precipitating cloud, just below one or more unsaturated downdrafts, and spreads out in the boundary layer. The potential energy

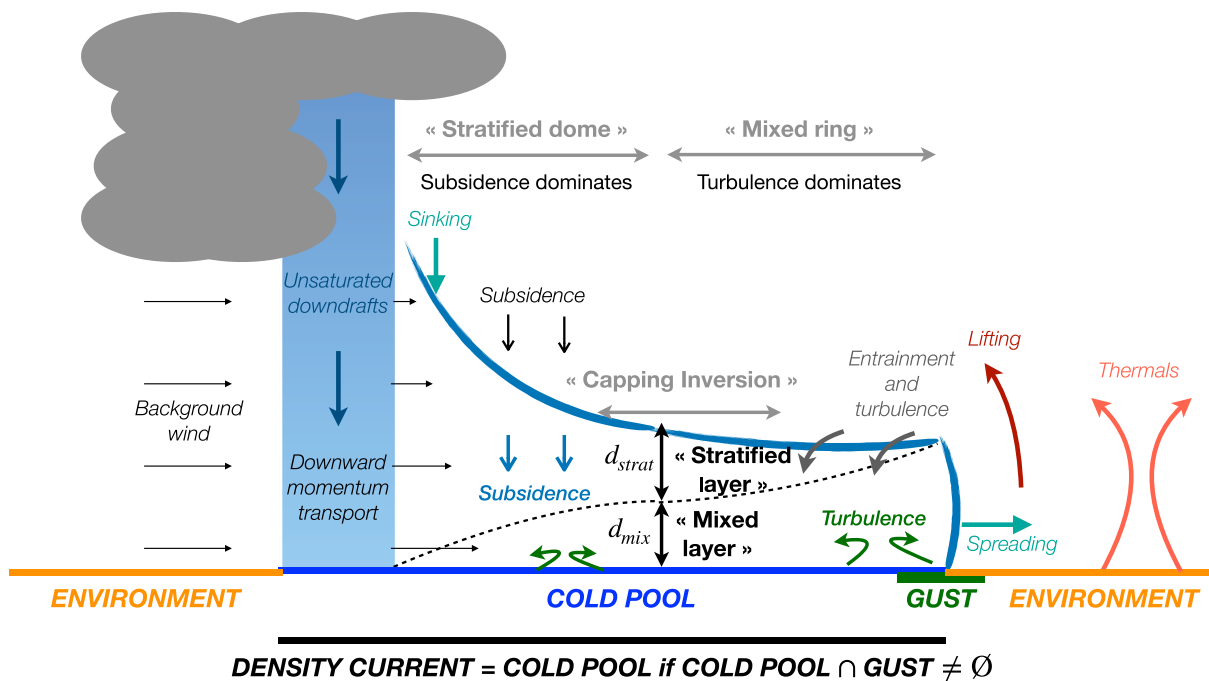


**Figure 1.** Conceptual picture of density currents. Key hypothesis: a density current is a cold pool adjacent to at least one gust front. Thick italic capitalized fonts designate the main regions that will be identified, thanks to the method presented in this study. Thin italic fonts refer to established features in the near environment of density currents. Semi-thick italic fonts refer to established features inside density currents. Thick black fonts are the assumed intrinsic properties based on physical arguments generalizing state-of-the-art knowledge on density currents occurring in deep convective regimes: these aspects can be seen as the main assumptions on which the proposed density currents' model relies. Thick gray fonts are the assumed additional properties of density currents; these aspects can be seen as nonsystematic but expected frequent features of the density currents were detected, thanks to our method.  $d_{mix}$  and  $d_{strat}$  refer, respectively, to the mixed layer depth and the stratified layer depth.

related to the overall negative buoyancy of the density current (sinking motion in the center) is converted into kinetic energy (spreading at the edges), enhancing turbulence close to the surface (by friction) and close to the gust. This rapid spreading generates lifting just ahead of the gust and subsidence above. The whole current forms a spatially and temporally coherent structure. It is the whole structure that we want to identify and characterize.

## 2.2. A Cold Pool Associated to a Wind Gust

Following these considerations, density currents can no longer be defined solely as a temperature anomaly with respect to a spatial mean at the surface (Gentine et al., 2016; Hirt et al., 2020; Torri et al., 2015), or from horizontal buoyancy variance (Drager & van den Heever, 2017), passive tracer concentrations (Romps & Jeevanjee, 2016) or even precipitating water (Torri & Kuang, 2019), as it was the case in these recent numerical studies. We define a density current as a cold pool, evidenced by a negative temperature perturbation, adjacent to one or several gust fronts (see Figure 1), evidenced by a negative temperature tendency. The latter approach is consistent with point-based observations where a temperature drop is used to assess the presence of a gust (see Section 1, de Szoeke et al., 2017; Zuidema et al., 2017). Defined like this, gusts are not solely the geometric contour of cold pools (e.g., like in Hirt et al., 2020), but rather reflect their leading edge, where wind bursts (e.g., the so-called “head-winds” by Simpson and Britter, 1980), moisture convergence (Fankhauser, 1976; Knupp, 2006; Weaver & Nelson, 1982) lifting processes (Miller, 1978; A. Thorpe et al., 1980), as well as dynamical interactions with the environment implying vorticity (M. W. Moncrieff & Miller, 1976; A. J. Thorpe & Miller, 1978) or collisions (Haerter, 2019; Hirt et al., 2020) are the most prominent.

### 2.3. Inside Density Currents: A Two-Layered, Two-Region Structure

In Figure 1, it is suggested that density currents encompass two vertical layers (one mixed, one stratified), and two regions (one mostly turbulent, the mixed ring, and one mostly subsident, the stratified dome). These features, although inspired from the vast literature, have never been tested against recent observations, nor in recent numerical studies, especially in the presence of shallow precipitating convection. This is the reason why these features appear *a priori* less established than those presented in the previous two Sections 2.1 and 2.2.

#### 2.3.1. Two Layers

The first hypothesis that we make is that density currents are made of two layers; a mixed layer topped by a stratified layer. This view has already been supported by conceptual frameworks partly inherited from GATE observations of tropical precipitating clouds (Gaynor & Ropelewski, 1979), MCS (Zipser, 1977) and squall-lines (Johnson & Nicholls, 1983) and taken over in cold pool parameterizations for GCM by Qian et al. (1998) and Grandpeix and Lafore (2010). In Figure 1, these two layers are separated by a black dashed line.

1. The mixed layer: the lowest layer is mostly turbulent as the rapid spread of the density current creates surface friction and enhances turbulence, similarly to a classical wind-induced surface layer. Since the strong turbulence near the surface mixes dry static energy, one may assume that, similarly to a dry convective PBL, the potential temperature  $\theta$  and the virtual potential temperature  $\theta_v$  are conserved in the mixed layer of depth  $d_{mix}$  and height  $h_{mix}$  above ground. One important thing to notice is that the mixed layer inside density currents only comprises a surface layer, where turbulence is shear-driven, where a typical mixed layer in a convective PBL usually comprises for a surface layer (small eddies) topped by a convective layer (coherent eddies). In the presence of density currents, we argue that the convective layer is canceled since there is no instability at the surface.
2. The stratified layer: on the other hand, the upper layer might experience subsidence due to mass conservation (Grandpeix & Lafore, 2010); as the density current spreads, it collapses. In observations, this subsidence may be an analogue to the so-called “mesoscale sinking” mentioned by Zipser (1977). The resulting strong stability might cancel the turbulent mixing over the depth  $d_{strat}$  of the resulting stratified layer, up to the height  $h_{strat}$ . In recent numerical studies, in which the analysis was focused on the ascending motions induced by lifting just ahead of the gust front (e.g., Hirt et al., 2020; Romps & Jeevanjee, 2016; Torri et al., 2015), subsidence induced by density current collapse has not been explored. But this phenomenon may be important to trigger and maintain dry clear-sky patches, where strong radiative cooling rates may favor long-lasting divergent circulations. Johnson and Nicholls (1983) observed very stable PBL at the rear of squall-lines, which could be maintained for several hours. In the density current parameterization developed by Grandpeix and Lafore (2010), the authors also stress the importance of this term. From these elements, and from the study of Gaynor and Ropelewski (1979), who showed that the inversion strength in the trades was strengthened after the passage of a wake, it is possible to conjecture that if the subsidence is strong enough, one can even expect to find a temperature inversion topping the density current stratified layer has to exist. This is what is suggested in Figure 1 with the “capping inversion.”

#### 2.3.2. Two Regions

From theoretical considerations, a density current is a gravity current (Klemp et al., 1994), clearly separated from the quiescent environment by the presence of a steep buoyancy discontinuity at its front materialized by a vigorous wind gust. Laboratory experiments (Charba, 1974; Simpson, 1969) and observations (Craig & Goff, 1976) pointed out that turbulence maximizes near the “nose” of the density current, just ahead of the “wake”, where the depth of the density current maximizes and turbulence is mostly driven by entrainment from the top. Hence, just behind the gust front, the density current is generally turbulent. However, when getting toward the center of divergence, the mixed layer depth decreases to reach a local minimum just behind the rainshaft, and increases again at the rear of the precipitating system as the PBL recovers (Johnson & Nicholls, 1983; Zipser, 1977). These elements support the presence of two distinct regions along a longitudinal section of a density current.



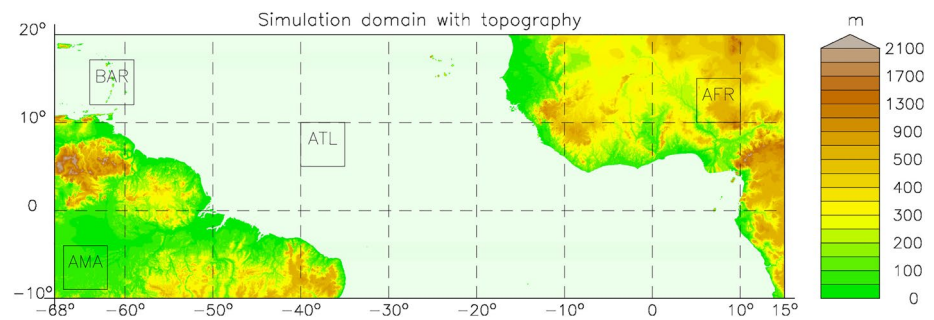


**Figure 2.** Computational domain of the ICOSahedral Non-hydrostatic (ICON) simulations with topography (shaded). The four regions of interest are also highlighted: AMA for Amazon ( $67^{\circ}$ – $62^{\circ}$ W: $9^{\circ}$ – $4^{\circ}$ S), AFR for Africa ( $5^{\circ}$ – $10^{\circ}$ E: $10^{\circ}$ – $15^{\circ}$ N), ATL for Atlantic ( $40^{\circ}$ – $35^{\circ}$ W: $5^{\circ}$ – $10^{\circ}$ N) and BAR for Barbados ( $64^{\circ}$ – $59^{\circ}$ W: $12^{\circ}$ – $17^{\circ}$ N).

1. The mixed ring: as density currents are generated by precipitating downdrafts that transport momentum downwards (Pantillon et al., 2015) and expand horizontally, they induce wind shear. However, the interaction of this intrinsic shear with environmental wind shear can cause strong vorticity anomalies close to the edge of the density current, and then enhances turbulence in the “rotor” region (Dudhia et al., 1987; A. Thorpe et al., 1982), right behind the “jump updraught” (M. W. Moncrieff, 1992). Moreover, starting from the center of divergence and approaching the gust front, frictional forces slow down the density current and increase its depth (Berson, 1958), which results in the characteristic 2D shape illustrated by Charba (1974) (see their Figure 11) and Wakimoto (1982) (see his Figure 3). This strongly turbulent region will be referred to as the mixed ring.
2. The stratified dome: close to the center of divergence, one may assume that the density current core interacts much less with the environment. In this *protected* region, much less low-level turbulence is expected. Moreover, the close presence of precipitating downdrafts induces an intense cooling which may strongly stabilize this region. This region will be referred to as the stratified dome.

#### 2.4. Approach and Structure of the Paper

The conceptual picture presented above will serve as a guideline to build up a methodology aimed at detecting density currents in simulations, that is, to “reveal” these coherent structures embedded in the turbulent flow. The word “reveal” must be thought as a synonym of “represent”, exactly like a parameterization represents—rather than mimics—a particular process. The structure of the paper is voluntarily held similar to the structure of a parameterization development paper: first a conceptual picture is proposed (Section 2); then an experimental setup is described (Section 3); a formulation, including some free parameters, is derived and implemented (Section 4), and its behavior is finally assessed over test cases (Section 5).

Let us finally make it clear that, in Section 4, only the so-called “intrinsic properties” shown in Figure 1, which make part of the density currents’ building blocks, are used to design the detection method; this concerns the cold pool, the gust, the environment, the mixed layer, and the stratified layer. And in Section 5, the so-called “additional properties” shown in Figure 1 are presented as emergent properties of density currents, diagnosed thanks to the detection method; this concerns the mixed ring, the stratified dome, and the capping inversion.

### 3. Data and Methodology

#### 3.1. Experimental Set-Up

We use the simulations conducted by Klocke et al. (2017) for our analysis. The simulations were performed in support of the Next-Generation Aircraft Remote Sensing for Validation (NARVAL) flight campaign and cover the Tropical Atlantic basin extending from  $68^{\circ}$ W to  $15^{\circ}$ E and from  $10^{\circ}$ S to  $20^{\circ}$ N (see Figure 2). The grid spacing, computed as the square root of the triangular grid cells area, amounts to 2.5 km. In the vertical, a stretched vertical coordinate is used with 75 layers, whereby 12 layers are located in the first kilometer. The simulations are conducted for the months of December 2013 and July 2016. They are started every day

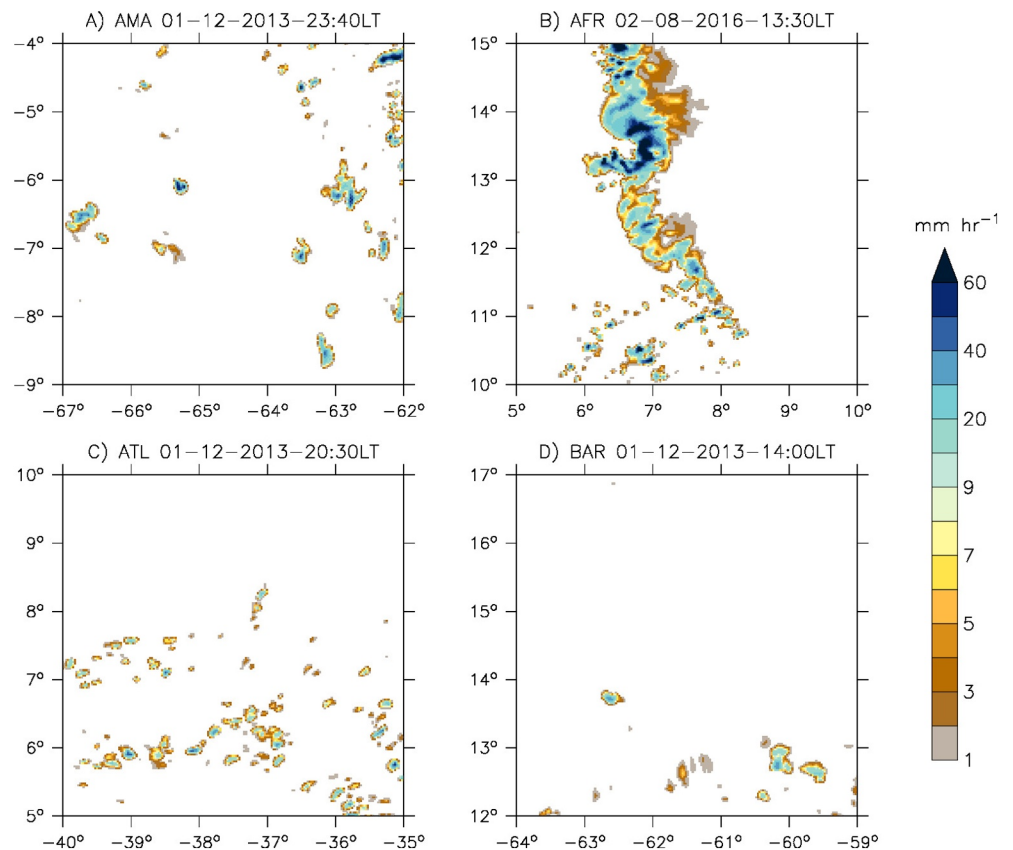


**Figure 3.** Maps of hourly accumulated surface precipitation ( $\text{mm h}^{-1}$ ) for (a) Amazon (AMA), (b) Africa (AFR), (c) Atlantic (ATL) and (d) Barbados (BAR) cases.

at 00 UTC from the analysis of the European Centre for Medium-Range Weather Forecasts (ECMWF) and integrated for 36 h. Boundary data are taken from the ECMWF forecasts and updated every 3 h. At the bottom boundary, the Sea Surface Temperature (SST) is taken from the ECMWF analysis. It is kept fixed at its initial value during the 36-h integration period. Over land, the surface temperature is fully interactive and uses the land-surface model from the German Weather Service (DWD), called TERRA.

The simulations were conducted using the ICOSahedral Non-hydrostatic (ICON) model (Zängl et al., 2015). Given the horizontal grid spacing, no convective parameterization is employed and convection is explicitly resolved by the bulk microphysics scheme that predicts cloud water, rain, snow, ice, and graupel (Baldauf et al., 2011). The parameterizations for gravity wave drag and subgrid-scale orography are also switched off, apart from that, the model employs the same parameterizations as the operational model version in use at the DWD, among which parameterizations for radiation and small-scale turbulence, see Zängl et al. (2015) and Klocke et al. (2017) for further details.

### 3.2. Analysis Methodology

To explain our detection procedure of density currents, we will first make use of four specific examples. Those were chosen to span different forms of convection as typically encountered in the tropics. The geographical location of the four regions is outlined in Figure 2 and the associated snapshots of precipitation are illustrated in Figure 3. All the domains cover an area of  $5^\circ$  by  $5^\circ$  for consistency.

The first two regions, called AMA as an abbreviation for Amazon and AFR as an abbreviation for Africa, are used as examples for convection developing over tropical land areas. AMA typifies the pop-corn like deep convection. Over the Amazon region, the convective inhibition energy is low, water is plentiful, and

convection easily develops during the wet season (Betts & Jakob, 2002). The convection reaches about 15 km, the convective cells are of small horizontal extent with an equivalent diameter of  $\sim 10$  km and the cells appear mostly randomly distributed. This distribution of convection stands in stark contrast to the distribution of convection in AFR. There, convective inhibition is high, the soil is dry and the convection organizes in a squall line due to the interactions between wind shear and cold pools (Parker & Diop-Kane, 2017). The multicellular system reaches a maximum height of 18 km and hosts convective cells of  $\sim 40$  km width.

The last two regions, ATL for equatorial Atlantic and BAR for the Barbados region, instead exemplify marine convection. ATL represents deep convection as encountered in the Intertropical Convergence Zone (ITCZ) over the Atlantic Ocean. The sharp transition between the ITCZ and the dry subtropics can be recognized around  $8^\circ$  in Figure 3c. Otherwise the characteristics of convection, with a vertical extent of 7–11 km, an equivalent diameter of  $\sim 5$  km, and a rather random distribution of cells, is reminiscent of the distribution of convection in AMA. In contrast, the BAR region has been chosen to sample a case with shallow to mid-level convection, with cloud tops ranging from 3 to 8 km. In this regime, it has been shown that clouds precipitate, produce cold pools, and are organized by them (Snodgrass et al., 2009). But since the model does not include a parameterization for shallow convection, results might be interpreted carefully for the BAR case, where PBL coherent structures are potentially misrepresented.

Local times are 23:40, 13:30, 20:30, and 14:00, respectively for the AMA, AFR, ATL, and BAR cases. Again, these different local times are meant to span a wide variety of cases in order to better extract the specific imprint of density currents. Having daytime and nighttime situations offers the possibility to compare density currents occurring in convective versus stable PBLs. Moreover, their behavior in the presence of a temperature inversion at the surface is, as far as we know, is something quite unexplored in recent studies, except in Knupp (2006) where the role of density currents in the triggering of solitary waves or bores in stable PBLs was studied.

## 4. From Boundary Layer Thermodynamics to Density Currents' Detection

### 4.1. Virtual Potential Temperature in the Mixed Layer

#### 4.1.1. Definition

In the conceptual model presented in Section 2, the rapid expansion of density currents generates strong turbulence in the PBL surface layer. Since this turbulence mixes the air very efficiently in the first atmospheric layers, one may expect to find a quasi-neutral  $\theta_v$  profile from the ground up to the height  $h_{mix}$ , especially in the region of the mixed ring (see Figure 1). The height of the mixed layer  $h_{mix}$  at any point is here taken equivalent to the PBL height  $h_{pbl}$  as in Canut et al. (2012):  $h_{mix}$  is the lowest altitude  $z$  above ground where  $\theta_v(z + dz)$  exceeds the mass-weighted average of  $\theta_v$  from the surface, at the altitude  $z_{sfc}$ , to  $z$  by a threshold of  $\epsilon = 0.2$  K. This gives:

$$h_{mix} = \min \left\{ z > z_{sfc}, \theta_v(z + dz) > \tilde{\theta}_v(z) + \epsilon \right\}$$

$$\text{with } \tilde{\theta}_v(z) = \frac{\int_{z_{sfc}}^z \rho(\xi) \theta_v(\xi) d\xi}{\int_{z_{sfc}}^z \rho(\xi) d\xi} \quad (1)$$

In the following, mass-weighted averages over  $h_{mix}$  of any intensive variable  $X$  will be denoted  $X_{mix}$ :

$$X_{mix} = \tilde{X}_{h_{mix}} = \frac{\int_{z_{sfc}}^{z_{sfc} + h_{mix}} \rho(z) X(z) dz}{\int_{z_{sfc}}^{z_{sfc} + h_{mix}} \rho(z) dz} \quad (2)$$

From that, we define the mixed-layer virtual potential temperature  $\theta_{v,mix}$ , which is displayed in Figure 4 for each snapshot selected from the NARVAL simulations. In Figure 4, it can be seen that  $\theta_{v,mix}$  exhibits strong spatial heterogeneities. Our hypothesis is that these heterogeneities mostly reflect the presence of density currents, whose spatial organization, shape and depth vary a lot from case to case. As expected,  $\theta_{v,mix}$  perturbations are larger over dry regions (i.e., land cases AMA and AFR) and when convection is deeper (i.e.,



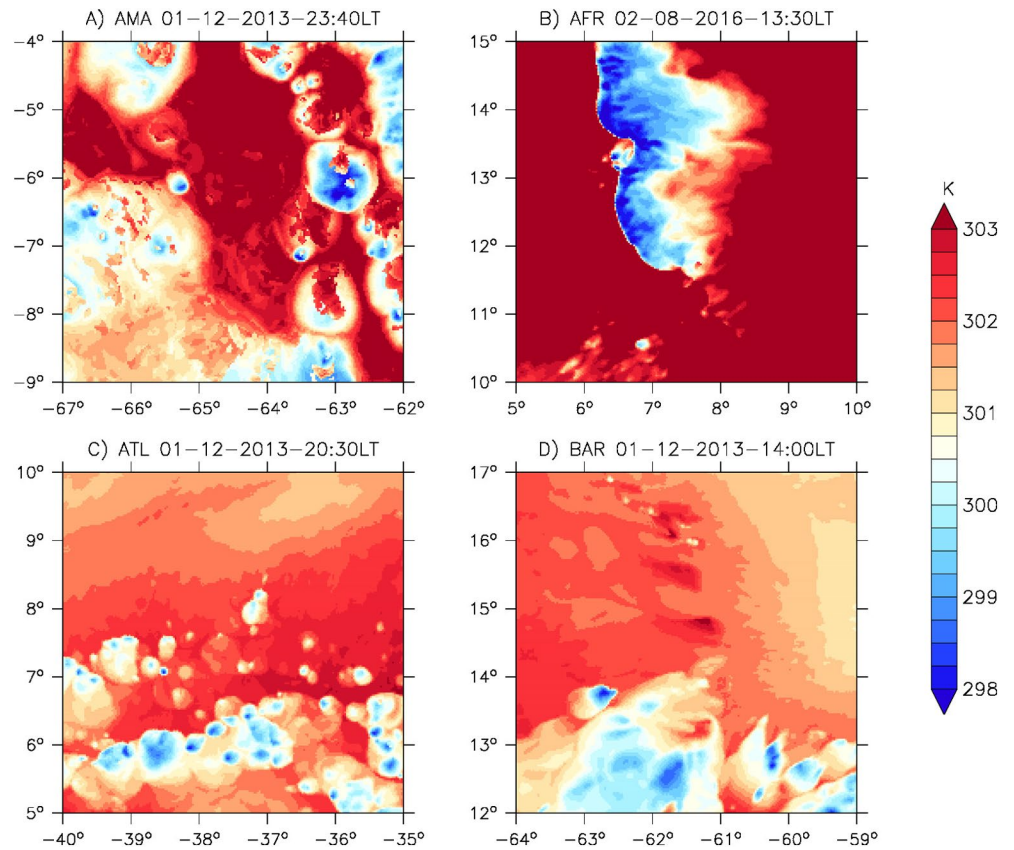


**Figure 4.** Maps of virtual potential temperature averaged over the mixed layer  $\theta_{v,mix}$  (shading, K) for the four cases.

AFR for land cases and ATL for ocean cases) because stronger convection produces more rain and drier PBL increases rain evaporation.

#### 4.1.2. On the Choice of $\theta_{v,mix}$ to Detect Cold Pools

Past studies have tended to use near-surface  $\theta_v$  to detect cold pools, for example, at 10 m, instead of its vertical average over the PBL. Here, in most cases,  $\theta_{v,10m}$  and  $\theta_{v,mix}$  maps are very similar (not shown). However, in Figure 5, some subtle but significant differences appear in the AMA case. The  $\theta_{v,mix}$  map

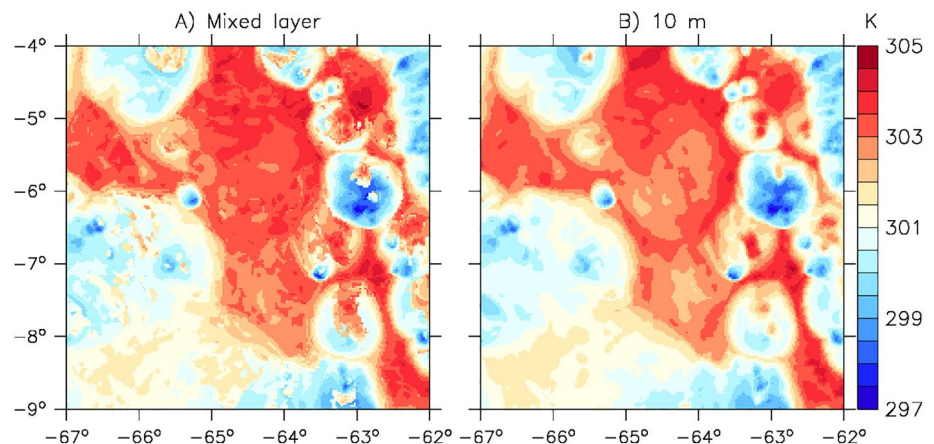


**Figure 5.** Maps of virtual potential temperature averaged over the mixed layer (left panel,  $\theta_{v,mix}$  shading, K) and at 10 m (right panel,  $\theta_{v,10m}$  shading, K) for the AMA case.

shows a warm anomaly at the center of the presumed density currents, giving the quasi-annular shapes. On the contrary, the  $\theta_{v,10m}$  map shows more uniform cold patterns. These differences are indeed caused by the presence of nocturnal surface temperature inversions. Similarly to the recovery of a convective PBL after the passage of a density current, during which surface fluxes and turbulence slightly build up the mixed layer back to its initial state after the passage of a density current, one could consider that, in the presence of a stable PBL, the surface inversion layer might also recover from the strong surface mixing induced by a density current. Hence, we assume that the presence of a nocturnal inversion at the center of the cold pool pattern reflects the recovery process taking place at a certain time after the passage of the density current.

This assumption requires to formally distinguish regions where surface cooling dominates, through radiative losses and/or surface evaporation, from regions where PBL cooling dominates, by advection caused by density currents. A way to achieve this goal is to consider  $\theta_{v,mix}$  rather than  $\theta_{v,10m}$ . Indeed,  $\theta_{v,mix}$  consistently reflects the low-level cooling by cold pools, but at the same time it also reflects the low level mixing induced by their spreading. Ultimately, this assumption is consistent with the statement of Section 2 that a density current must consist of a mixed layer topped by a stratified layer. Any region where a temperature inversion is found at the surface is thus viewed either “undisturbed” or “recovering” and is not part of density current.

To discriminate density currents from cold surfaces topped by a temperature inversion, we define the height of the surface inversion  $h_{inv,sfc}$  as the first height above ground where the vertical gradient of temperature becomes negative:

$$h_{inv,sfc} = \min \left\{ z > z_{sfc}, \frac{dT(z)}{dz} < 0 \right\} \quad (3)$$

Regions where  $h_{inv,sfc} > 0$  are not part of a density current.

In Figure 6a,  $h_{inv,sfc}$  is mapped for the AMA case. Strong surface inversions, reaching 100–200 m in height, are simulated at 22:40 LT, especially in quiescent areas (e.g., location 1 in Figure 6a). These inversions are absent where density currents seem to be spreading (e.g., location 2 in Figure 6a). This result clearly illustrates the ability of density currents to efficiently mix the first atmospheric layers. Looking into more details, other surface inversions appear right at the center of the presumed density currents (e.g., location 3 in Figure 6a). In Figures 6b and 6c, vertical profiles of temperature  $T$  and virtual potential temperature  $\theta_v$  are plotted at locations 1, 2, and 3. These profiles suggest that low level mixing is a robust characteristic of density currents, up to the point that density currents even induce a slight heating of the surface ( $T_{2,surf} \geq T_{3,surf}$ ) and prevent location 2 from nighttime inversion (at least temporarily).

Concerning location 3, the surface temperature inversion might be caused by the combination of two factors: (i) a remaining surface cooling induced by recent precipitation or the recent passage of a density current, and (ii) a remaining strong subsidence motion aloft driven by the density current dynamics (see Figure 1). This has to be investigated in more detail, but if this assumption is correct, location 3 might reflect the track of a density current that has already gone away; its imprint on the surface temperature still remains but its imprint on the atmosphere already disappeared. Such particular regions cannot be defined strictly as “density currents” following our conceptual model, as they are devoid of a mixed layer, however, one can advance that specific inversions could reflect a “collapsed density current”, not forcibly related to surface cooling but rather generated by a strong subsidence induced by the recent passage of a density current. In fact, similar surface inversions were also found close to the center of density currents in the ATL case (not shown). This intriguing feature might deserve a particular attention in future studies.

In any case,  $\theta_{v,mix}$  is found to be a robust variable to reveal the strong mixing of the surface layer, which is characteristic of density currents spreading over rough surfaces. In the following, we will use this variable to detect the track of density currents in various situations. The choice of  $\theta_{v,mix}$  allows to identify regions experiencing a surface cooling strictly resulting from the passage of a density current, rather than other cooling processes such as evaporation or radiation.

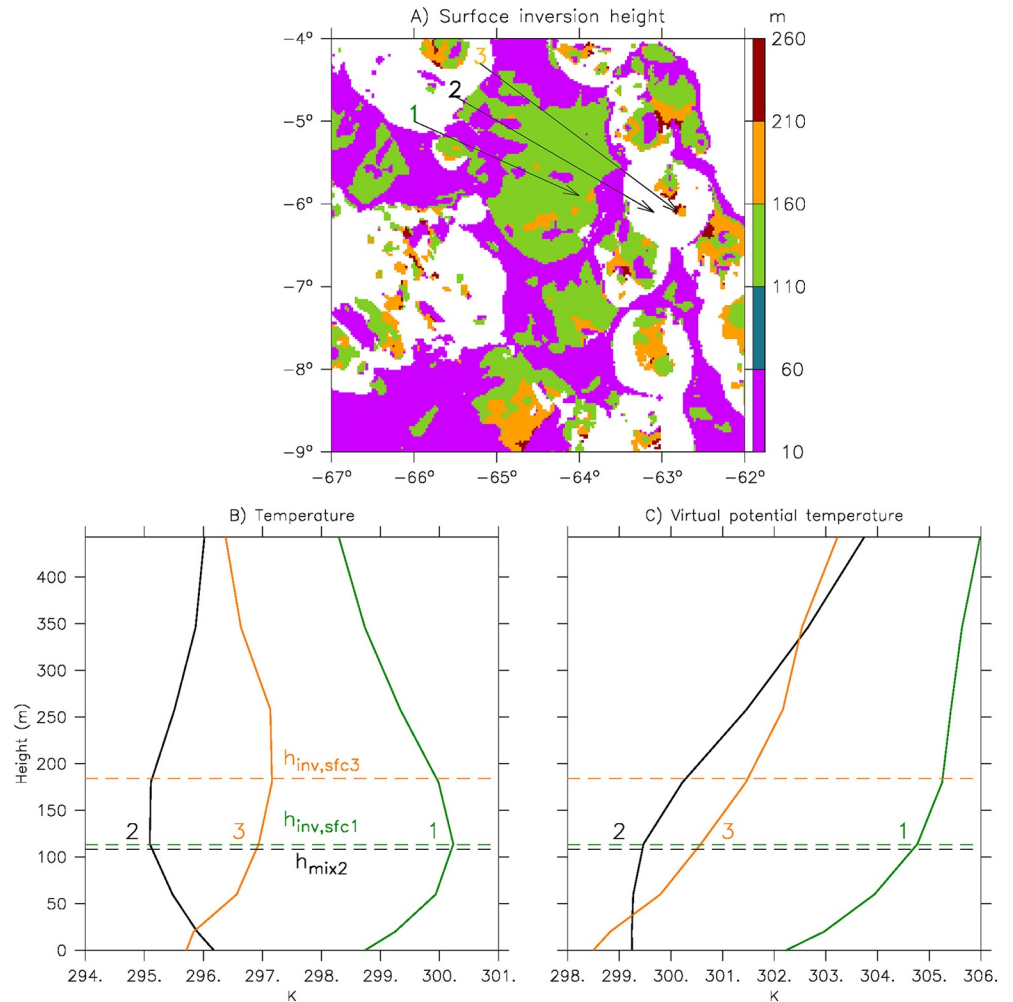


**Figure 6.** (a) Map of surface inversion height  $h_{inv,sfc}$  (shading, m). Vertical profiles of (b) temperature  $T$  (K) and (c) virtual potential temperature  $\theta_v$  (K) over locations 1 (green solid, quiescent nighttime PBL), 2 (black solid, density currents) and 3 (orange solid, recovering nighttime PBL) for Amazon (AMA).

#### 4.1.3. Cold Anomalies With Respect to Domain-Mean $\overline{\theta_{v,mix}}$

The core feature of the density current in our definition is its cold pool: it is a negative temperature anomaly with respect to a reference value. In some recent studies using convection-permitting simulations, this reference value is taken as the temperature spatially averaged over the domain of study (Gentine et al., 2016; Hirt et al., 2020; Torri et al., 2015). We tested this approach in Figure 7, which illustrates the cold pool mask (named COLD) and the environmental mask (named ENV) that are obtained from taking the anomaly from an horizontal average. A mask for gusts (named GUST) is also illustrated even if the definition of gusts is delayed to the next section (see Equation 9).

First, by construction, imposing  $\theta_{v,mix} < \overline{\theta_{v,mix}}$  for cold pool detection imposes  $f_{cold} \simeq 0.5$  in all cases. Moreover, in Figure 7, very large regions identified as cold pools do not actually match the precipitation pattern. Despite the fact that density currents can travel far away from the precipitating downdrafts they come from, in our view, they must have been initially connected to a downdraft itself close to a precipitation event. Hence, their spatial distribution should better match that of surface precipitation. Finally, gust fronts do not match cold pool boundaries in Figure 7, except in AFR where the discontinuity is very strong and only associated with one single, very large cold pool.

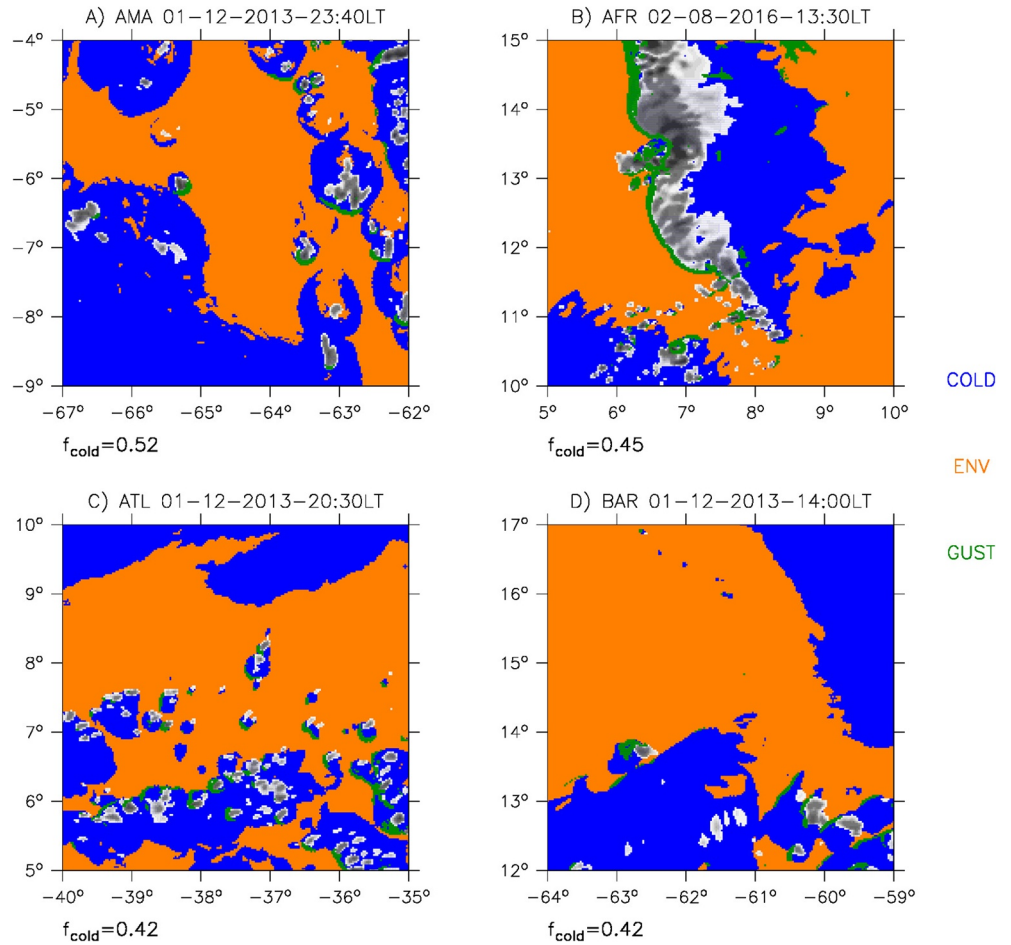


**Figure 7.** Maps of the two regions of the domain for the four cases. COLD refers to the cold pools (blue shading), that is, where  $\theta_{v,mix} \leq \overline{\theta_{v,mix}}$ . ENV refers to the cold pools environment (orange shading), that is, where  $\theta_{v,mix} > \overline{\theta_{v,mix}}$ . The GUST region is defined later in Equation 9, but has just an indicative sense at this stage. Hourly accumulated surface precipitations are represented in gray shading (inverse greyscale,  $Pr > 1 \text{ mm}^{-1}$ ). Below each panel the cold pools fractional coverage in the domain  $f_{cold}$  is displayed.

From this simple example, one can understand why the use of such an approach often requires to be complemented by additional criteria (e.g., precipitation, tracer concentration, etc.) to get more realistic cold pool detections. Given these limitations, our objective is instead to base the temperature anomaly on a reference value that is (i) less sensitive to the size of the study domain and (ii) more closely related to intrinsic properties of density currents. For that, we first need to define the gust front. To tackle this issue, we take advantage of observational studies.

## 4.2. Gust Fronts

### 4.2.1. Definition

As already stressed in Section 1 (de Szoeke et al., 2017; Zuidema et al., 2017), in most in-situ observations, density currents are primarily detected from the presence of a gust passing through a stationary sensor (de Szoeke et al., 2017; Provod et al., 2016; Zuidema et al., 2017). In these studies, the gust is perceived as a sudden temperature drop of about  $10^{-3} \text{ K s}^{-1}$  magnitude, associated with wind bursts. In order to be consistent with these observational considerations, we define the gust as:

$$\text{GUST} = \left\{ (x, y) \in \mathcal{D}, \frac{dT_{sfc}(x, y)}{dt} \leq \gamma \right\}, \text{ with } \gamma = -10^{-3} \text{ K s}^{-1} \quad (4)$$



and  $\mathcal{D}$  being the study domain. Now the goal is to connect Equation 4 to  $\theta_{v,mix}$ , rather than  $T$ , as  $\theta_{v,mix}$  is our primary variable used to detect the density current.

First, the energy conservation equation is applied to an air layer just above the surface. In Jacobson (2005), Equation 3.66 gives:

$$\frac{d\theta_{v,sfc}}{dt} = \frac{\partial\theta_{v,sfc}}{\partial t} + (\vec{U}_{sfc} \cdot \vec{\nabla})\theta_{v,sfc} = \frac{\theta_{v,sfc}}{c_{p,d}T_{v,sfc}} \frac{dQ}{dt} = \frac{\theta_{v,sfc}}{c_{p,d}T_{v,sfc}} \dot{Q} \quad (5)$$

where  $\vec{U}_{sfc}$  is the wind vector at the surface,  $c_{p,d}$  is the heat capacity of dry air and  $Q$  is the enthalpy. Close to the surface, one can neglect the vertical wind component  $W_{sfc}$  with regard to the horizontal ones ( $U_{sfc}$ ,  $V_{sfc}$ ). We can then assume  $\vec{U}_{sfc} = \vec{U}_{sfc} + \vec{V}_{sfc}$  for the wind vector.

The diabatic heating term  $\dot{Q}$  can be split in; (i) a cooling term  $\dot{Q}_{rain}$  accounting for rain evaporation close to the unsaturated downdrafts; (ii) heating and cooling terms  $\dot{Q}_{sens}$  and  $\dot{Q}_{lat}$  accounting for sensible and latent heat fluxes strengthening at the passage of the density current (because of turbulence and temperature contrast enhancement between the surface and the first atmospheric layer) radiative term  $\dot{Q}_{rad}$  accounting for radiative exchanges. The diabatic term in Equation 5 is thus rewritten as:

$$\dot{Q} = \dot{Q}_{rain} + \dot{Q}_{rad} + \dot{Q}_{sens} + \dot{Q}_{lat} \quad (6)$$

At this stage, three hypotheses are formulated:

1. Concerning  $\dot{Q}_{rad}$ , radiative effect can be neglected considering the short timescales involved in the density current's gust lifecycle.
2. Concerning  $\dot{Q}_{rain}$ , unsaturated downdrafts cover a small fraction of the storm (Emanuel, 1991), hence the cooling due to rain evaporation can be neglected with respect to horizontal transport. This is particularly true close to the gust, which is the furthest point from unsaturated downdrafts (see Figure 1). This gives  $(\vec{U}_{surf} \cdot \vec{\nabla})\theta_{v,surf} \gg \dot{Q}_{rain}$  in Equation 5.
3. Concerning  $\dot{Q}_{sens}$  and  $\dot{Q}_{lat}$ , surface fluxes can be very important underneath cold pools. Gentine et al. (2016) have shown in numerical simulations that surface fluxes tend to heat and moisten cold pools. For simplicity, we nevertheless neglect this contribution. As surface fluxes tend to heat cold pools, our detection method will provide a lower bound on the number and total area covered by the gusts.

In summary, we assume that the horizontal advection term dominates the heat budget, that is, that the density current rapid expansion acts to cool the environmental PBL more than anything else, and write:

$$\frac{\partial\theta_{v,sfc}}{\partial t} = -(\vec{U}_{sfc} \cdot \vec{\nabla})\theta_{v,sfc} \quad (7)$$

Let us now consider a tropical atmosphere, with  $T_{sfc} = 300$  K,  $q_{v,sfc} = 1.5 \cdot 10^{-2}$  kg kg<sup>-1</sup> and crossed by a gust in which  $\frac{\partial T_{sfc}}{\partial t} = -10^{-3}$  K s<sup>-1</sup>,  $\frac{\partial q_{v,sfc}}{\partial t} = -10^{-5}$  kg kg<sup>-1</sup> s<sup>-1</sup> (these values are rough estimates from observed time series in de Szoeke et al. (2017); Zuidema et al. (2017); Vogel et al. (2021)). From these observed values, one can suppose  $\frac{\partial\theta_{v,sfc}}{\partial t} \approx \frac{\partial T_{sfc}}{\partial t}$ .

Finally, as the mixed layer homogenizes  $\theta_v$  over its depth,  $\theta_{v,sfc} \approx \theta_{v,mix}$ , and similarly for time variations, it follows that  $\frac{\partial\theta_{v,mix}}{\partial t} \approx \frac{\partial\theta_{v,sfc}}{\partial t}$ . In order to guarantee consistency between the  $\theta_v$  and  $\vec{U}$  fields, one may also assume homogeneity for the horizontal wind field over the mixing depth  $d_{mix}$ , such that  $\vec{U}_{sfc} \approx \vec{U}_{mix}$ . This assumption is strong knowing that, in the mixed layer, frictional forces create strong wind shear, which itself causes turbulence in the surface layer. However, we decided to make the choice to let this aspect aside in order to ensure consistency for the advection term computation. Under these assumptions, Equation 7 is finally rewritten as:

$$\frac{\partial\theta_{v,mix}}{\partial t} = -(\vec{U}_{mix} \cdot \vec{\nabla})\theta_{v,mix} \quad (8)$$



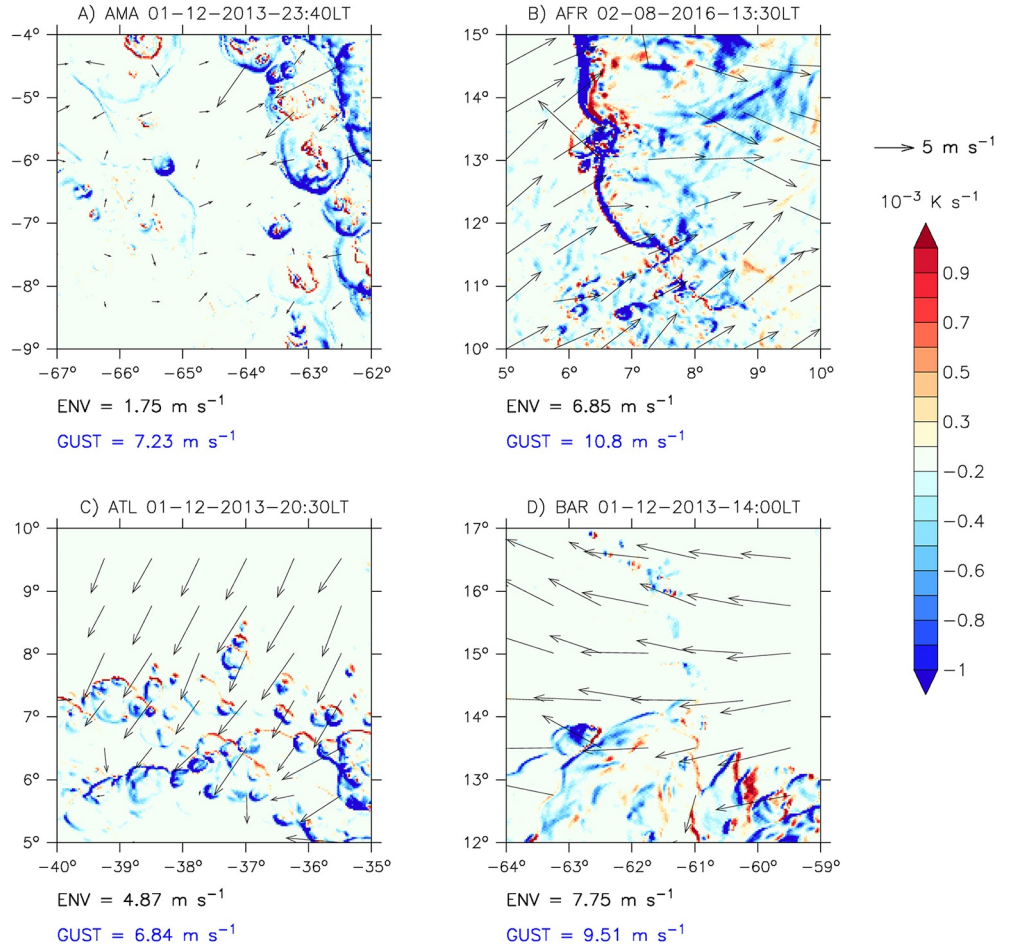


**Figure 8.** Maps of horizontal advection term  $-\bar{U}_{mix} \cdot \bar{\nabla} \theta_{v,mix}$  (shading,  $K s^{-1}$ ) and mixed layer background (i.e., outside from density currents) wind vectors  $\bar{U}_{mix}^{env}$  ( $m s^{-1}$ ) for the four cases. Saturated blue regions correspond to gusts, where  $-(\bar{U}_{mix} \cdot \bar{\nabla}) \theta_{v,mix} \leq -10^{-3} K s^{-1}$ . At the bottom of each panel the mixed layer wind strength averaged over the area outside of density currents  $\|\bar{U}_{mix}^{env}\|$  (in black) and the mixed layer wind strength averaged over the area covered by the gusts  $\|\bar{U}_{mix}^{gust}\|$  (in blue) are given.

Ultimately, the whole gust region, denoted GUST in the following, encloses the points verifying the following criterion, adapted from Equation 4, where a centered finite difference scheme is used to discretize  $\nabla$ :

$$GUST = \left\{ (x, y) \in \mathcal{D}, \quad -(\bar{U}_{mix}(x, y) \cdot \bar{\nabla}) \theta_{v,mix}(x, y) \leq \gamma \right\} \quad (9)$$

#### 4.2.2. Identified Gust Fronts in the Four Test Cases

In Figure 8, saturated blue regions are gusts as defined using Equation 9. The relative orientation of these gusts with respect to the large-scale wind gives a qualitative information on the direction of propagation of density currents; gusts exhibit an arcus-like structure whose convex side indicates their direction of propagation. However, their shape and their direction of propagation vary with large-scale and surface conditions.

Overall, land cases have larger, but less frequent gusts than oceanic cases. In the quasi-absence of large scale flow (i.e., AMA case), gusts exhibit an annular shape, materializing a quasi-circular divergent flow spreading in all directions. On the contrary, in the presence of strong wind shear (i.e., AFR case), gusts are merged together into a single quasi-linear squall line. In this case, the resulting propagation is upwind with respect to the low level monsoon flow. Interestingly, when looking more closely at the AFR case, we can also notice

small density currents ahead of the main squall line, perhaps related to recently triggered storm cells, and whose direction of propagation is opposite from that of the squall-line.

In the ATL case, gusts seem to propagate orthogonally to the trade winds. In the BAR case though, gusts are mostly oriented downwind, with trade winds significantly stronger ( $\sim 8 \text{ m s}^{-1}$ ) than in the ATL case ( $\sim 5 \text{ m s}^{-1}$ ). Again, without providing a rigorous explanation for this, one may advance that the convection regime (i.e., shallow or deep) explains these differences. For instance, momentum transport by unsaturated dowdraughts highly depends on the wind shear they experience along the vertical. Therefore, the resulting direction of propagation of the gusts with regard to the low level wind depends on the level they originate, and hence on the depth of convection. Figure 8 also reveals heating anomalies at the rear of density currents, more or less at the opposite side of gusts. These local heatings are due to warm air advection by the large-scale flow over cooled areas, which have already experienced density currents.

For each snapshot, we also displayed the average gust velocity  $\|\vec{U}_{mix}^{gust}\|$ , noted  $\overline{U}_{mix}^{gust}$  for simplicity, in the lower right corner of each panel of Figure 8. This velocity is obtained by averaging  $\|\vec{U}_{mix}^{gust}\|$  over the surface  $\Omega_{gust}$  covered by all the gust fronts in each snapshot:

$$\overline{U}_{mix}^{gust} = \frac{1}{\Omega_{gust}} \int_{\Omega_{gust}} \|\vec{U}_{mix}^{gust}\| d\Omega \quad (10)$$

This variable is thought to provide an instantaneous estimate of the mean propagation speed of the gusts, which is an interesting proxy to estimate their lifting energy for instance (Grandpeix & Lafore, 2010). For the AFR case the propagation speed provided by  $\overline{U}_{mix}^{gust} \sim 10.8 \text{ m s}^{-1}$  (see Figure 8) is consistent with typical values of squall lines propagation velocity in the Sahel region, which ranges roughly from 10 to 15  $\text{m s}^{-1}$  (Grandpeix et al., 2010; Provod et al., 2016). Moreover, in the AFR case, estimating directly the speed of this squall line through its tracking over successive snapshots (not shown), yields a similar propagation velocity of  $\sim 13 \text{ m s}^{-1}$ .

Therefore, one can make the assumption that, at a given time, the density current propagation speed  $\langle c_{dens} \rangle$  averaged over the density current population scales with the mean gusts velocity  $\overline{U}_{mix}^{gust}$  averaged over the area covered by the gusts:

$$\langle c_{dens} \rangle \approx \overline{U}_{mix}^{gust} \quad (11)$$

This assumption is strong as it includes the translational speed of cold pools, but it has the great advantage to avoid the use of two, or more, consecutive snapshots to estimate the density current propagation speed.

Now that the density current leading edges (i.e., the gust fronts) are detected through a relevant, physically based criterion, they can be used to design a reference value to compare with and thereby detect cold pools.

#### 4.2.3. Cold Pool Definition From Gust Properties

The reference temperature from which anomalies will be computed to define the cold pool must be such that part of the gust cells are colder than this reference value. In Figure 9, for each snapshot, the cumulative distribution function of  $\theta_{v,mix}$  in the gusts ( $\text{CDF}(\theta_{v,mix}^{gust})$ , in green) is compared with the cumulative distribution of  $\theta_{v,mix}$  in the whole domain ( $\text{CDF}(\theta_{v,mix})$ , in black).

First, we notice that the  $\theta_{v,mix}^{gust}$  range is very similar to the  $\theta_{v,mix}$  range. This supports the idea that gusts are straddling the two regions: cold pools and their environment. They represent thus a relevant sample of the thermodynamic state of the whole domain. Second, the  $\text{PDF}(\theta_{v,mix}^{gust})$  is skewed toward cold values. This asymmetric distribution is very likely linked to the presence of cold pools. In order to capture this tail, we make the arbitrary choice to set the reference temperature,  $\theta_{v,mix}^{ref}$ , to the first quartile  $Q_1$  of the  $\theta_{v,mix}^{gust}$  distribution:

$$\theta_{v,mix}^{ref} = Q_1(\text{PDF}(\theta_{v,mix}^{gust})) \quad (12)$$

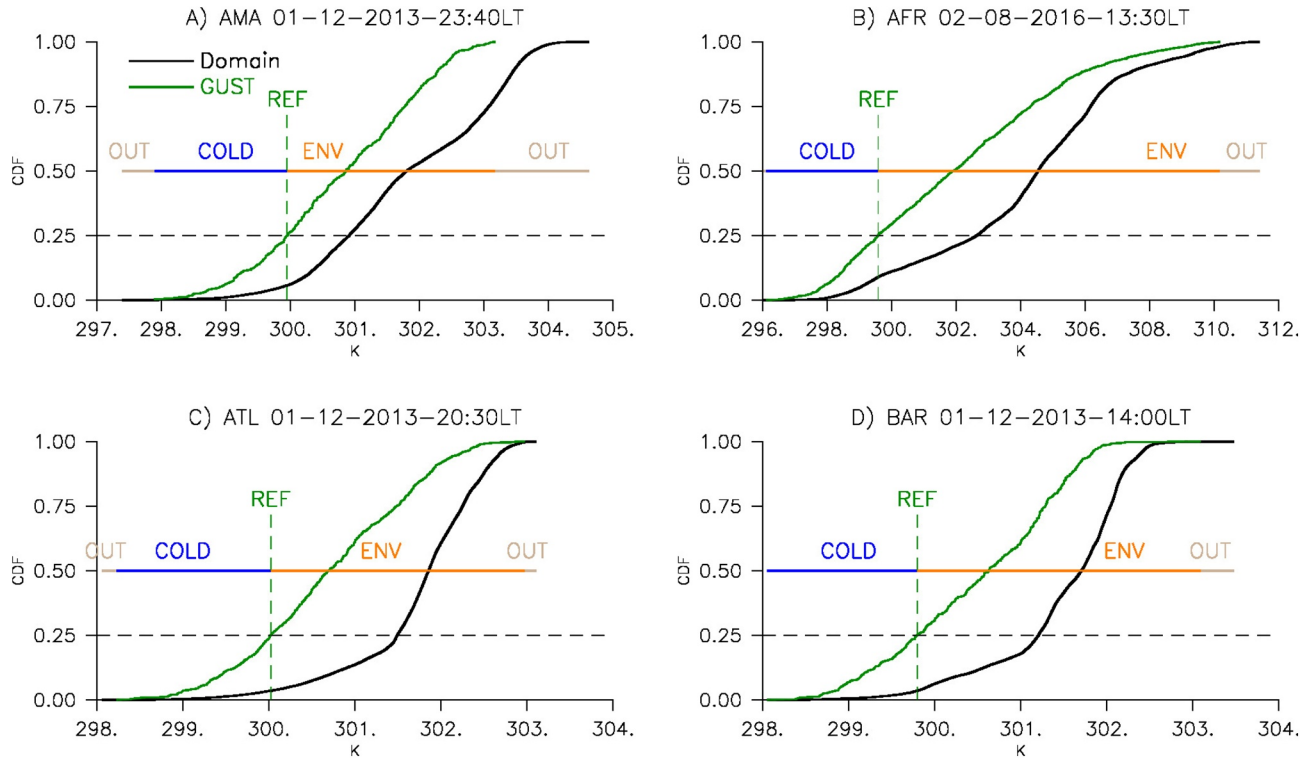


**Figure 9.** Cumulative distribution functions of  $\theta_{v,mix}$  in the whole domain ( $CDF(\theta_{v,mix})$ , black solid) and in the gust zone ( $CDF(\theta_{v,mix}^{gust})$ , green solid) for the four cases. The reference temperature  $\theta_{v,mix}^{ref}$  is defined as the first quartile of  $CDF(\theta_{v,mix}^{gust})$  (green dashed). COLD refers to the cold pools, that is, where  $\text{Min}\{\theta_{v,mix}^{gust}\} \leq \theta_{v,mix} \leq \theta_{v,mix}^{ref}$ . ENV refers to the cold pools environment, that is, where  $\text{Max}\{\theta_{v,mix}^{gust}\} \geq \theta_{v,mix} > \theta_{v,mix}^{ref}$ . OUT refers to the cold pools outer region, that is, where  $\theta_{v,mix} < \text{Min}\{\theta_{v,mix}^{gust}\}$  and  $\theta_{v,mix} > \text{Max}\{\theta_{v,mix}^{gust}\}$ .

With this choice, cold pools are locations where  $\theta_{v,mix} < \theta_{v,mix}^{ref}$ . Note that this approach considers the gust properties rather than those of the whole domain. Consequently, it filters out most of the sources of  $\theta_{v,mix}$  spatial variance other than those associated with density currents. It is thus less sensitive to the domain size than other cold pool detection methods and better suited for the problem at hand. The choice of the first quartile rather than another quantile in Equation 12 was done empirically as it allowed to detect cold pools in a wide range of situations, including in a regime with shallow convection over an oceanic surface (i.e., the BAR case). A sensitivity analysis has been performed to assess this choice (not shown). As expected, increasing this threshold enhances the cold pool fractional coverage, but their number does not increase in a monotonous way. This is because cold pool structures tend to merge when they get larger.

Concerning the external region outside cold pools, a distinction is made between the outer region—denoted OUT—, defined where  $\theta_{v,mix} < \text{Min}\{\theta_{v,mix}^{gust}\}$  or  $\theta_{v,mix} > \text{Max}\{\theta_{v,mix}^{gust}\}$ , and the environment adjacent to cold pools—denoted ENV—, defined where  $\text{Max}\{\theta_{v,mix}^{gust}\} \geq \theta_{v,mix} > \theta_{v,mix}^{ref}$ . Consequently, only the  $\theta_{v,mix}$  range found in the gusts matters for characterizing cold pool internal properties and their interactions with the adjacent areas. Any hypothetical cold region in the OUT region will not be counted as a cold pool. However, an important limitation appears when cold pools and gusts are present on both sides of a large-scale thermodynamic heterogeneity (e.g., an SST front). In that particular case, since the range of temperatures encountered in the gusts reflects two distinct environments, using it to capture cold pools may favor the detection of one cold pool population rather than the other one. This is the reason why this methodology should be applied carefully in large domain sizes, in which several cold pool populations might be embedded into distinct large-scale environments.

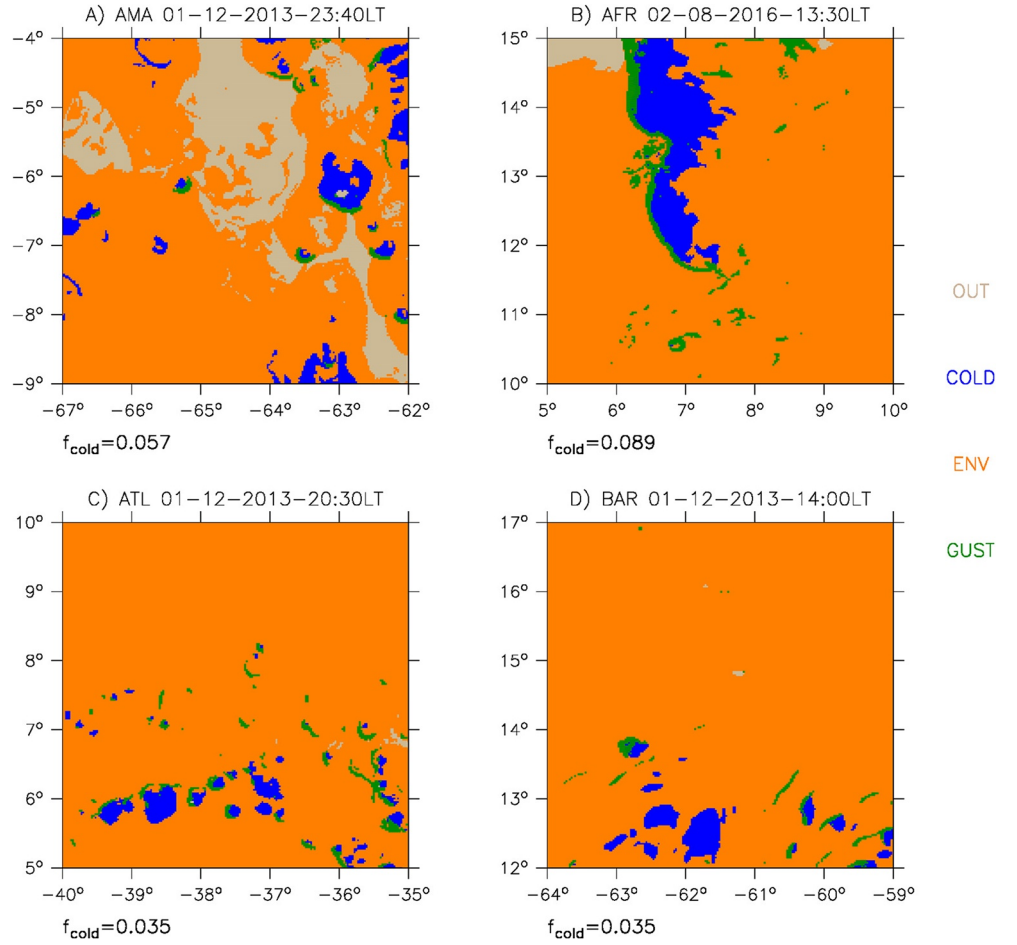


**Figure 10.** Same as in Figure 7 but following Equation 14 for the definition of COLD, ENV, GUST regions, and with additional OUT region. The cold pools fractional coverage in the domain  $f_{cold}$  is displayed below each panel.

Ultimately, the COLD region is defined as:

$$\text{COLD} = \left\{ (x, y) \in \mathcal{D}, \quad \min\{\theta_{v,mix}^{gust}\} \leq \theta_{v,mix}(x, y) \leq \theta_{v,mix}^{ref} \right\} \quad (13)$$

### 4.3. Cold Pools

Four regions were defined through the preceding sections, as summarized in Equation 14. These masks were applied on the four cases and the results are displayed in Figure 10.

$$\begin{aligned} \text{GUST} &= \left\{ (x, y) \in \mathcal{D}, \quad -(\bar{\mathcal{U}}_{mix}(x, y) \cdot \bar{\nabla}) \theta_{v,mix}(x, y) \leq \gamma \right\} \\ \text{OUT} &= \left\{ (x, y) \in \mathcal{D}, \quad \theta_{v,mix}(x, y) \leq \min\{\theta_{v,mix}^{gust}\} \text{ or } \theta_{v,mix}(x, y) \geq \max\{\theta_{v,mix}^{gust}\} \right\} \\ \text{COLD} &= \left\{ (x, y) \in \mathcal{D}, \quad \min\{\theta_{v,mix}^{gust}\} \leq \theta_{v,mix}(x, y) \leq \theta_{v,mix}^{ref} \right\} \\ \text{ENV} &= \left\{ (x, y) \in \mathcal{D}, \quad \theta_{v,mix}^{ref} \leq \theta_{v,mix}(x, y) \leq \max\{\theta_{v,mix}^{gust}\} \right\} \end{aligned} \quad (14)$$

Compared to Figure 7, identified cold pools in Figure 10 are well colocated with moist convection events. Gusts are also more frequently located at the cold pool boundaries. This result supports the self-consistency of the hypothesis assuming a gust acting as a buffer zone between the environment and the cold pool, in which subcloud processes like lifting, moisture convergence, and enhanced surface fluxes participate in the generation of new clouds. The gusts are, overall, very narrow (their width hardly exceeds 10 km), but

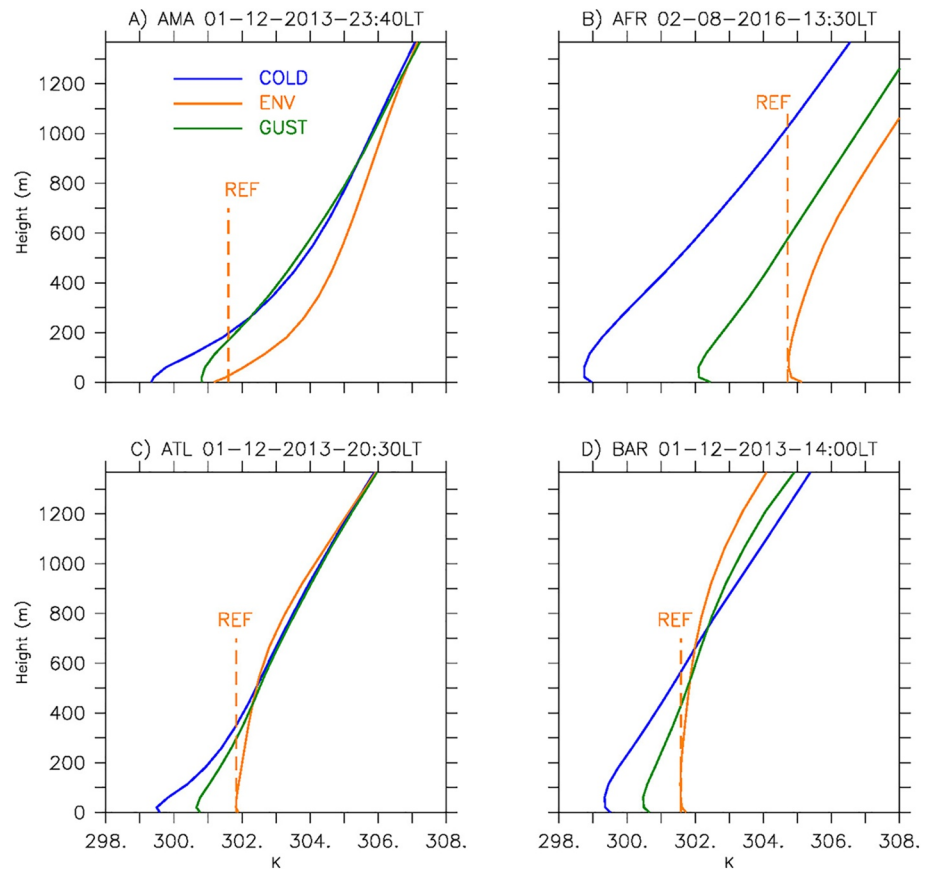


**Figure 11.** Vertical profiles of  $\theta_v$  (K) spatially averaged over the COLD region ( $\overline{\theta_v^{cold}}$ , blue solid), over the ENV region ( $\overline{\theta_v^{env}}$ , orange solid) and over the GUST region ( $\overline{\theta_v^{gust}}$ , green solid) for the four cases. The reference temperature is defined as  $\theta_{v,mix}^{env}$  (orange dashed, see Equation 15).

again, subtle differences among cases show that their horizontal extent is positively correlated with cold pool dimensions. Moreover, looking at Figure 10, cold pools fractional coverage  $f_{cold}$  is very different from one case to another.  $f_{cold}$  now appears as a fully independent variable, not anymore constrained to be close to 0.5. Overall,  $f_{cold}$  is smaller in oceanic cases, in which convection exhibits a “pop-corn” structure. Over land, as the atmosphere is drier and rain evaporation is stronger, convection is scarcer and produces less frequent, but larger cold pools. In the AFR case, there is a typical squall-line situation in which a single cold pool covers a significant fraction of the domain.

Finally, one may also notice that isolated gusts and isolated cold pools can be present in Figure 10: some cold pools are not surrounded by any gust and, conversely, some gusts are not connected to any cold pool. It is perfectly consistent to consider that some gusts may not be related to any cold pool. Indeed, a marked breeze front can generate a significant temperature drop without being connected to any precipitating cloud. However, in the present case, these features rather resemble gust fronts disconnected from decaying clouds (Wakimoto, 1982) or solitary waves (Knupp, 2006). Equivalently, in Figure 10, cold pools without gusts may simply reflect a local negative surface temperature anomaly due to (i) a recent rainfall event, (ii) the recent passage of a density current, or (iii) being related to a strong radiative cooling pattern. But since our conceptual model defines a density current as a cold pool adjacent to one gust at least (see Figure 1), all these isolated features are not identified as density currents, so that the fractional coverage  $f_{dens}$  is always smaller than  $f_{cold}$ .

By considering a reference temperature computed from the gust properties, a more consistent cold pool mask was designed, providing estimates of  $f_{cold}$  more sensitive to the large-scale forcing and to the



convective development stage, and less constrained by the domain size as with previous methodologies. At this stage, we are now able to detect the density current lower layer (mixed layer), the boundaries (gusts) and core (cold pools) of density currents. The next step is to define the upper layer, that is, the “stratified layer” and, hence, the vertical extent of density currents.

#### 4.4. The Stratified Layer

Subsident motions inside density currents result from mass-conservation (Grandpeix & Lafore, 2010), that is, the fact that as density currents spread they collapse, and from the unsaturated downdrafts feeding them (Zipser, 1977), that is, through rain evaporation. One may expect to find a stratified layer on top of the mixed layer. The next task in the detection procedure is to estimate the depth  $d_{strat}$  of this layer. To do so, let us analyze the mean thermodynamic profiles of the different regions that were already defined as COLD, ENV, and GUST.

Figure 11 displays the vertical profiles of  $\theta_v$  spatially averaged over the COLD ( $\overline{\theta_v^{cold}}$ , in blue), ENV ( $\overline{\theta_v^{env}}$ , in orange) and GUST ( $\overline{\theta_v^{gust}}$ , in green) regions. It is worth saying that the absence of prominent mixed layers in these profiles comes from the spatial averaging of mixed layers of various heights. As such, these profiles provide information on the mean buoyancy contrast between the different regions but do not forcibly compare with individual point-based profiles taken in these regions. However, it can clearly be stated that; (i) the PBL is more developed in the ENV region than anywhere else; (ii) the mean buoyancy contrast between cold pools and their environment is by far the strongest in the AFR case; (iii) the mean properties of the gusts lie in between those of COLD and ENV regions; (iv) and the COLD region is, on average, more stratified than everywhere else.

Hence, we assume that, at every location  $(x, y)$  inside the COLD region, the upper limit of the density current  $h_{top}$  corresponds to the height above ground where  $\theta_v(x, y)$  is the same as the mean  $\theta_v$  of the mixed layer averaged in the ENV region (i.e.,  $\overline{\theta_{v,mix}^{env}}$ , dashed orange line in Figure 11). By doing so, we assume that, inside the COLD region,  $h_{top}(x, y)$  corresponds to the upper limit of the negative  $\theta_v$  (i.e., buoyancy) anomaly with regard to the mean  $\theta_v$  profile of the ENV region. To compute  $h_{top}$ ,  $\overline{\theta_{v,mix}^{env}}$  is used as a reference temperature ( $\theta_{v, strat}^{ref}$ ) to define the top of density currents. One has to be aware that this approach might bias the estimate of  $h_{top}$  to too low values, as the  $\overline{\theta_v^{env}}$  profile tends to minimize the estimate of  $\overline{\theta_{v,mix}^{env}}$  (because of the “mean-effect” evoked in the previous paragraph). We have then:

$$\forall (x, y) \in \text{COLD}, \quad h_{top}(x, y) = \min \left\{ z > z_{sfc}, \quad \theta_v(z) = \theta_{v, strat}^{ref} = \overline{\theta_{v,mix}^{env}} \right\} \quad (15)$$

Finally,  $d_{strat} = h_{top} - h_{mix}$ . With the determination of the vertical extent of the density current, the first four steps of the detection method are complete. Let's now define the PBL height  $h_{pbl}$ , both inside and outside density currents. In the ENV region, following Canut et al. (2012), we assume that  $h_{pbl} \simeq h_{mix}$  for convective PBLs. For stable PBLs, we assume that the PBL height corresponds to the inversion height  $h_{inv,sfc}$  in the ENV region. Finally, in the COLD region, we assume that the PBL top corresponds to the density current upper limit, that is, the sum of the mixed and the stratified layers.  $h_{pbl}$  is hence given by:

$$\begin{cases} (x, y) \in \text{ENV and } h_{inv,sfc} > 0 & \Rightarrow h_{pbl} = h_{inv,sfc} \\ (x, y) \in \text{ENV and } h_{inv,sfc} = 0 & \Rightarrow h_{pbl} = h_{mix} \\ (x, y) \in \text{COLD} & \Rightarrow h_{pbl} = h_{top} = d_{mix} + d_{strat} \end{cases} \quad (16)$$

which can also be written under the unified form:

$$(x, y) \in \mathcal{D} \Rightarrow h_{pbl} = h_{inv,sfc} + d_{mix} + d_{strat} \quad (17)$$

The final step, labeling each detected density current as an individual object in the snapshots, will be described in the next section.

#### 4.5. Density Currents' Definition

As stated in Section 2, a density current consists of a cold pool adjacent to, at least, one gust. The ensemble made of all density currents of the domain is named DENS. Its formal definition is as follows:

$$\text{DENS}^i = \{(x, y) \in \text{COLD}^i \text{ and } \exists j \text{ such as } \text{GUST}^j \cap \text{COLD}^i \neq \emptyset\} \quad (18)$$

A segmentation algorithm is used to tag every cold pool in contact with one or several gusts as a density current. First, the two-dimensional binary COLD mask constructed from the  $\theta_{v,mix}$  field is segmented; connected cells are labeled with the same unique identifier. A rule of four-connectivity is applied, that is, a pixel is connected to its neighbor if they share an edge. No threshold in size is imposed. The segmentation software is a python module based on the scipy ndimage library (<https://docs.scipy.org/doc/scipy/reference/ndimage.html>), that was previously used in Brient et al. (2019) and that is available online (<https://gitlab.com/tropics/objects>). Once the cold pools are uniquely identified, they are reviewed and selected as density currents only if at least one cell in the cold pool is non-zero in the GUST binary mask. Note that, since this segmentation is only made in space but not in time, splitting and merging processes are ignored. In the perspective of tracking density currents in time, the present method would necessarily have to take these processes into account.

Lastly, we designed a filtering method to extract relevant density current populations only and avoid capturing artifacts. In fact, if strong PBL heterogeneities are present in the domain and if the PBL located on the cold side of the heterogeneity is topped by a strong stable layer, such regions are labeled as density currents, although they are obviously not (not shown). As far as we could see in the ICON-NARVAL simulations, in these situations, the method computes very large density current fractions  $f_{cold}$  without any rain in the domain. These situations do not represent the majority of the cases, but are sufficiently frequent to significantly bias the detection method. To filter them out, we make the assumption that, by construction, gust fronts only cover a tiny fraction of the density currents. This is actually well demonstrated by Figure 12. One can also assume that  $d_{mix} > d_{strat}$  close to the gust fronts, but everywhere else  $d_{mix} \leq d_{strat}$ . In the next section (Section 5), Figure 13, Figure 14 and Figure 15 clearly show the validity of this statement. By combining these two assumptions, we assume that in a given domain, a density current population must have an area-averaged stratified layer  $\overline{d_{strat}^{dens}}$  deeper than its area-averaged mixed layer  $\overline{d_{mix}^{dens}}$ :

$$\overline{d_{strat}^{dens}} \geq \overline{d_{mix}^{dens}} \quad (19)$$

The main limitation of this filtering method is that it does not apply to each object separately, but to the whole population at once.

Similar to Figure 10, Figure 12 shows that density currents have different shapes and sizes regarding the case considered. But Figure 12 also adds interesting nuances. We still clearly see that over land, density currents are larger. Nevertheless, they are not necessarily less frequent than over ocean, as it was the case when considering cold pools only, in Figure 10. In the BAR case for instance, only a small fraction of cold pools are tagged as density currents. Interestingly, in that case, the largest cold pools are devoid of gust. It seems to be the opposite situation in all the other cases, where the largest cold pools are frequently tagged as density currents. Thus, one can see that the distinction we introduced between cold pools, density currents, and gust objects paves the way to a more accurate analysis of convective organization in convection-permitting models.

## 5. Analysis of the Identified Density Currents

### 5.1. Thermodynamic Features of Density Currents

In this section, features of the boundary layer are analyzed and related to the detected density currents in the four cases, and compared to the conceptual picture proposed in Section 2.

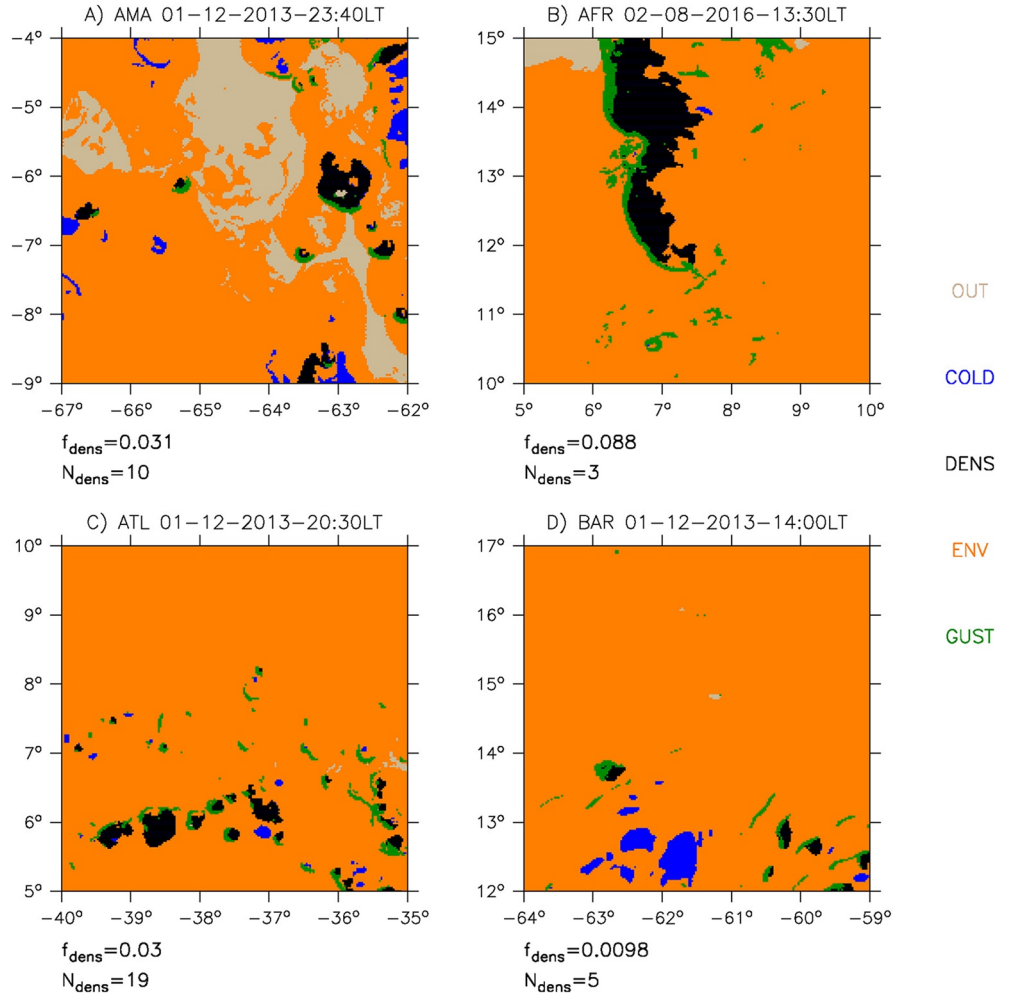


**Figure 12.** Same as Figure 10 with DENS referring to the density currents (black shading) as defined in Equation 18. The density current number  $N_{dens}$  and their fractional coverage  $f_{dens}$  are displayed below each panel.

### 5.1.1. Mixed Layer Depth $d_{mix}$ : Consistency of the Segmentation Algorithm

From  $h_{inv,sfc}$  (Equation 3) and  $h_{mix}$  (Equation 1), the depth of the mixed layer  $d_{mix}$  can be defined as:

$$d_{mix} = h_{mix} - h_{inv,sfc} \quad (20)$$

$d_{mix}$  is plotted in Figure 13. The density current population (black contours in Figure 13) does not exactly match the  $d_{mix}$  pattern. Indeed, the number and the size of density currents tagged in the domain is sensitive to the choice of (i) the parameter  $\gamma$  used to define the GUST region in Equation 9, and (ii) the parameter  $\theta_{v,mix}^{ref}$  used to define the COLD region in Equation 13.  $d_{mix}$  perturbations which are not related to density currents may result from local cooling processes or from cold pools devoided of gusts. Nevertheless, it can be stated that, overall, every density current (black contours in Figure 13) is collocated with a strong heterogeneity in  $d_{mix}$ . Density currents are either collocated with strong negative anomalies of  $d_{mix}$  in convective PBLs (see AFR, ATL, and BAR cases), or collocated with strong positive anomalies of  $d_{mix}$  in the presence of a nighttime surface inversion (see AMA case). The spatial correlation between density current objects and  $d_{mix}$  anomalies supports the consistency of the methodology built from the conceptual picture of Section 2. Here, Figure 13 supports the assumption that density currents strongly mix the surface layer. The next step is to analyze the features of the stratified layer inside the density current.

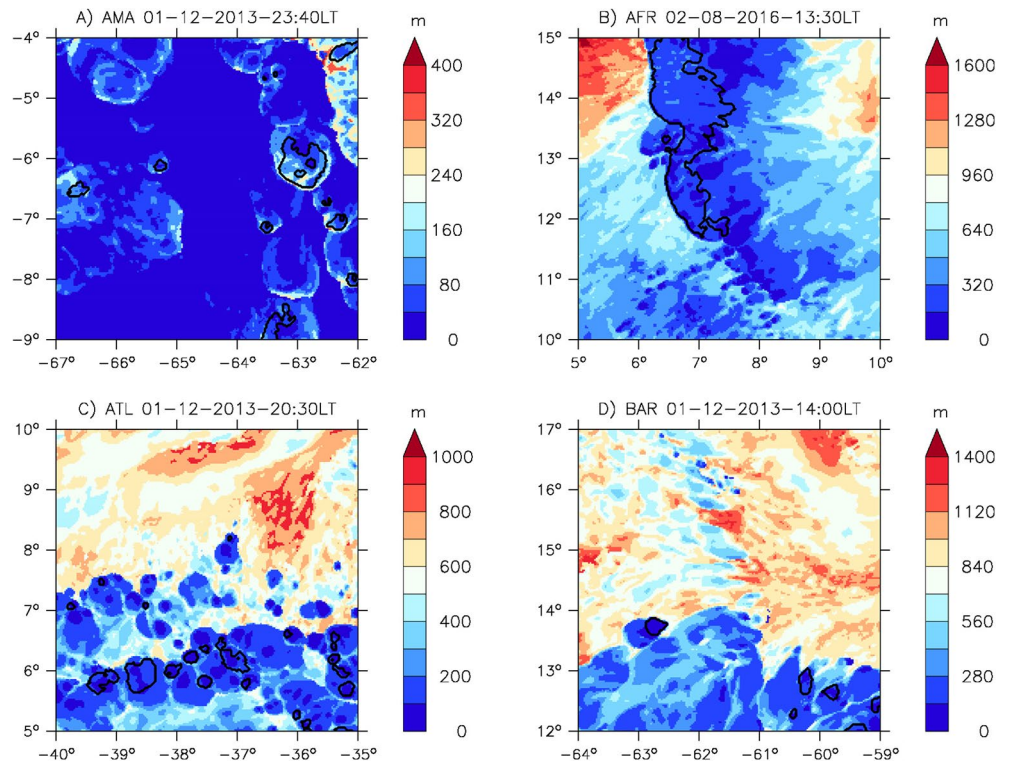


**Figure 13.** Maps of mixed layer depth  $d_{mix}$  (shading, m) for the four cases. Density currents are contoured in black.

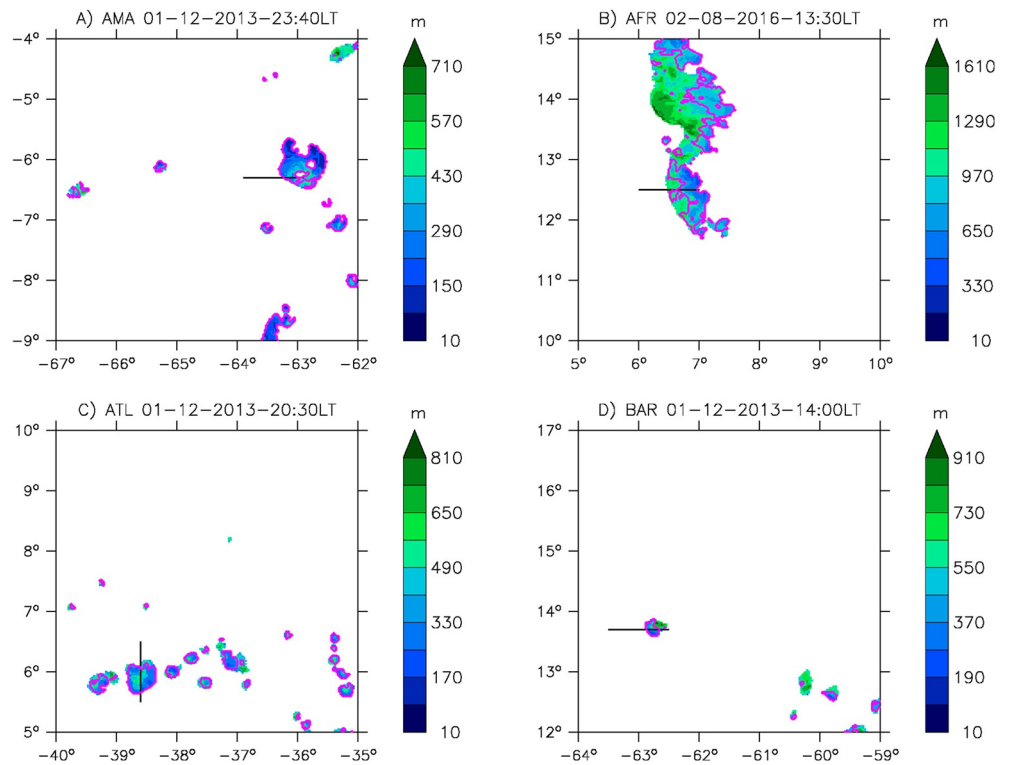


**Figure 14.** Maps of the stratified layer depth  $d_{strat}$  (shading, m) in the DENS region for the four cases. Purple contours delimit areas inside which a temperature inversion is present at the top of the stratified layer. Black solid lines refer to the specific transects analyzed in Figure 15.

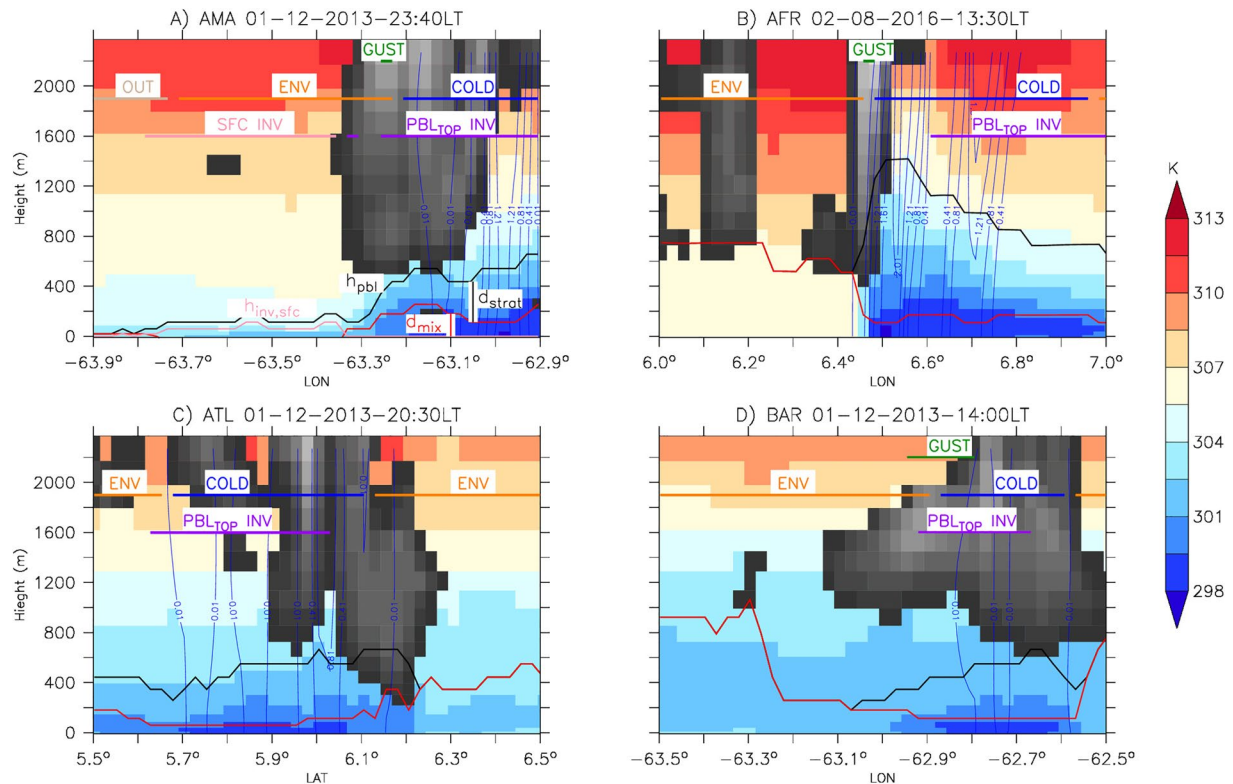


**Figure 15.** Vertical cross-section of  $\theta_v$  (shading, K) along specific transects displayed in Figure 14 for the four cases. Cloud condensed water (liquid and ice) mixing ratio ( $q_c + q_i \geq 10^{-2} \text{ g kg}^{-1}$ ) are in inverse greyscale shading. Precipitation (rain and snow) mixing ratio ( $q_r + q_s \geq 10^{-2} \text{ g kg}^{-1}$ ) is in blue contours. Black solid lines refer to the PBL top  $h_{pbl}$  (see Equation 17). Red solid line in panel (a) illustrates the mixed layer depth  $d_{mix}$ . Black vertical solid line in panel (a) illustrates the stratified layer depth  $d_{strat}$ . Pink dashed lines refer to the height of the surface inversion layer  $h_{inv,sfc}$ . The blue lines delimit the COLD regions, the orange lines delimit the ENV regions, the green lines delimit the GUST regions, and the gray lines delimit the OUT regions (see Equation 14). The purple lines highlight regions where a temperature inversion layer is present at PBL top, denoted “PBL<sub>top</sub> INV”. The pink lines highlight regions where a temperature inversion is present at the surface, denoted “SFC INV”.

### 5.1.2. Stratified Layer Depth $d_{strat}$

In Figure 14, maps of the stratified layer depth  $d_{strat}$  are plotted in the DENS region. As expected, the stratified layer is significantly deeper in the AFR case compared to others because the PBL is deeper and drier; the very large squall line includes a cold pool of more than 1.5 km depth. But interestingly, the purple contours in Figure 14 also show that temperature inversions are found at the top of the stratified layer for the vast majority of the detected density currents. This result supports the idea that subsiding motions in the stratified layer might, in some cases, be strong enough to generate temperature inversions, as suggested in Figure 1. To the best of our knowledge, the presence of such capping inversions at the top of density currents has never been studied yet. Another interesting point is that  $d_{strat}$  is larger close to the center of the density currents than at their edge, especially in the AMA and ATL cases. This feature will be further investigated in Section 5.1.3, but it supports the existence of the stratified dome evoked in Section 2.

### 5.1.3. Vertical Structure of Four Selected Density Currents

In order to have a closer look at the vertical structure of density currents, vertical cross-sections along four 100-km transects are displayed in Figure 15.

First, Figure 15 shows that the detected objects exhibit the horizontal structure suggested in Figure 1. The presence of a “Stratified dome” below the rainshaft is prominent in all the selected transects.  $d_{strat}$  is maximum in the region close to the density current center, where unsaturated dowdrafts strongly cool the PBL and the surface. In the stratified dome, the mixed layer is very thin but it gets deeper closer to the edge (i.e., the gust); it is the “Mixed ring” proposed in Figure 1. The abrupt step in  $d_{mix}$  can be attributed to the strong



turbulent mixing near the gust front. Overall, Figure 15 shows that the density current height  $h_{top}$  approximately scales with the cloud base height  $h_{cl}$ . Actually, the assumption that  $h_{top} \simeq h_{cl}$  is in line with results from the density current parameterization of Grandpeix and Lafore (2010) used in the GCM LMDZ (Hourdin et al., 2020). Over oceans, ongoing work with simulations performed with the model SAM (M. F. Khairoutdinov & Randall, 2003) in RCE and with fixed SST (personnal communication with Caroline Muller, LMD) rather suggests  $h_{top} \simeq 0.5h_{cl}$ . From Figure 15, one can see that the AFR case is very characteristic of a powerful squall-line, in which the associated cold pool appears as a sharp discontinuity (here  $\Delta T_{surf} \sim 8$  K), very much comparable with observed squall-lines during the AMMA campaign (Provod et al., 2016). This well-developed cold pool lifts low level air parcels very efficiently. This lifting effect triggers and feeds the new deep cell just ahead, right above the gust front. Strong positive vertical velocities are indeed simulated at this particular location (not shown).

Finally, as already stressed in Figure 14, most of the area covered by density currents seems capped by a temperature inversion (see purple line in Figure 15), supporting the view of Figure 1, where a capping inversion have been hypothesized. While it cannot be stated at this stage that these characteristics are always related to density currents, it is worth noting that similar structures were found in other simulated cloud scenes (not shown).

In summary, these transects first confirm the self-consistency of the conceptual picture presented in Figure 1: intrinsic properties such as the mixed layer and the stratified layer, from which the detection method has been derived, are prominent in all cases. Second, the additional properties anticipated in Figure 1 such as the mixed ring, the stratified dome, and the capping inversion were confirmed as well. Although these features were never (as far as we know) formally labeled like this before, these characteristics are not new (perhaps excepting the capping inversion) as they were explicitly or implicitly pointed out in other past studies. However, the present method offers for the first time the possibility to reveal them consistently in high-resolution simulations, thus opening the way to their reinvestigation with current numerical tools.

To further assess the consistency of the present methodology, its behavior over time and its sensitivity to spatial resolution are now analyzed.

## 5.2. Density Currents' Statistics

So far, we have been able to identify density currents in snapshots generated by a convection-permitting simulations in various contexts. Thanks to the specific labeling of density currents, quantitative information such as their number  $N_{dens}$  and their spatial coverage  $f_{dens}$  could be derived. Also using  $\overline{U_{mix}^{gust}}$  as a proxy for estimating the average density current propagation speed  $\langle c_{dens} \rangle$  (see Equation 11), we can extract a quantitative information on their strength. Moreover, mean equivalent radius  $\langle r_{dens} \rangle$  (i.e., obtained if similar cold pools were covering the same fraction of space) over the density currents' population can be easily deduced from their spatial density  $D_{dens} = \frac{N_{dens}}{\Omega_D}$ :

$$\langle r_{dens} \rangle = \sqrt{\frac{f_{dens}}{\pi D_{dens}}} = \sqrt{\frac{f_{dens} \Omega_D}{\pi N_{dens}}} \quad (21)$$

### 5.2.1. General Behavior in a 6-Day Time Series

In the following paragraphs, the temporal evolution of density current statistics over a 6-day period is analyzed for each case. The time series displayed in Figure 16 are built from hourly snapshots and are smoothed over a 2-h time window.

First, Figure 16 shows that times series are not overly noisy. The presence of high frequency fluctuations would have been the sign of inconsistencies in the definition of the density currents, as their individual life cycle generally exceeds hourly timescales, and even more if we account for the whole population. In the present cases, the introduced filtering criteria (see Equation 19) avoid these fluctuations. Indeed, when density currents artifacts are detected, very strong fluctuations appear in the time series (not shown). Hence, the breaks in the time series either correspond to periods without density currents, or correspond to periods

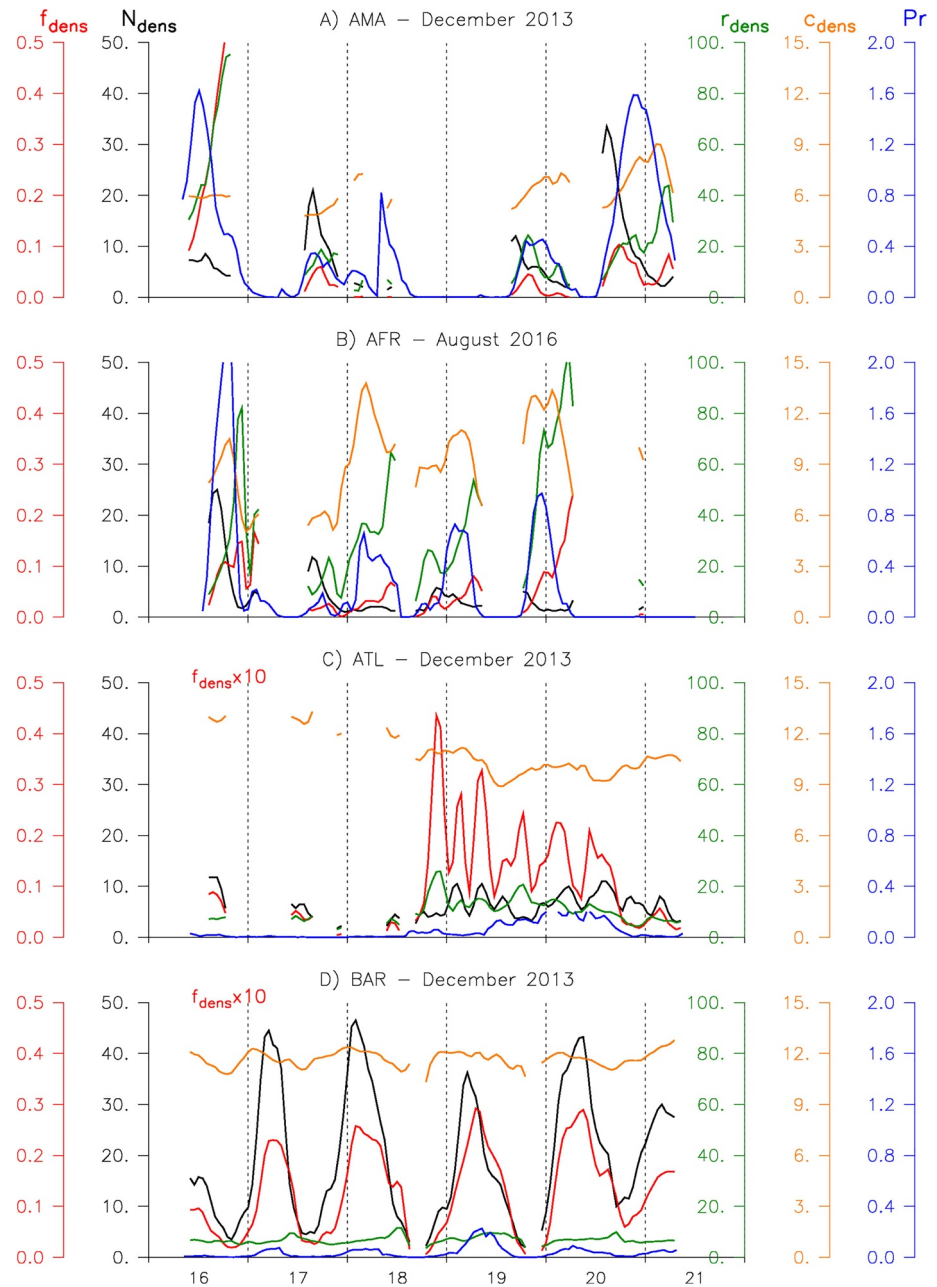


**Figure 16.** Time series (local time) of density currents' fractional coverage  $f_{dens}$  (red solid), density currents' number  $N_{dens}$  (black solid), average density currents' equivalent radius  $\langle r_{dens} \rangle$  (km, green solid), average density currents' gust velocity  $\langle c_{dens} \rangle$  ( $\text{m s}^{-1}$ , orange solid), and domain-mean surface rain rate  $\overline{Pr}$  ( $\text{mm hr}^{-1}$ , blue solid). In order to reveal  $f_{dens}$  time variations in oceanic cases,  $f_{dens}$  is scaled by a factor 10 in panel (c and d). Time series are built from hourly snapshots and then smoothed with a 2-h time window. Whenever the threshold  $\overline{d_{strat}^{dens}} \geq \overline{d_{mix}^{dens}}$  is not verified, density currents-related metrics are excluded. The vertical black dotted lines show the midnights LT for each simulation day.

during which artifacts are present. The absence of high frequency noise has also been checked on other time periods in the ICON-NARVAL simulations (not shown).

At the domain scale, the occurrence of density currents overall correlates with surface precipitation. However, although surface precipitation generally accompanies density currents, we recall that surface precipitation is neither a necessary nor a sufficient condition for their presence. In fact, when light

precipitation evaporates before reaching the surface in a dry PBL, density currents can develop without significant surface rain. Reversely, when almost no rain evaporation occurs in a very moist PBL, significant surface precipitation might not produce density currents. Here, in some cases, surface precipitation is not associated with any density current (e.g., AMA case the 18th of December) and, reversely, a significant number of density currents occur in the absence of significant surface precipitation (e.g., ATL case the 16th and 17th of December). The present method is able to capture this key nuance. Indeed, except for the BAR case, density current statistics do not perfectly correlate in time with surface precipitation intensity.

Overall, it seems that larger density current spatial coverage and larger radius are found in the land cases. This probably results from deeper convection (due to seasonality and/or location) associated with deeper PBLs over drier surfaces, in which evaporation of raindrops in the subcloud layer is more important.

But from a case-by-case analysis, more statements and conjectures can be formulated:

1. In the AMA case, no clear correlation between domain-mean surface precipitation  $\overline{Pr}$  and density current proxies can be seen. However,  $f_{dens}$  seems to correlate with  $\langle r_{dens} \rangle$ . This could be the sign of either an organized convection regime, in which  $f_{dens}$  is mostly controlled by density current merging processes, or a scattered—or “Pop-corn”—regime in which each density current grows on its own. Focusing on the 16th of December, the rapid increase of  $f_{dens}$  and  $\langle r_{dens} \rangle$  before convection stops can be interpreted as the signature of a growing mesoscale convective system getting out of the study domain. The same phenomenon can be seen on the 20th of December in the AFR case.
2. In the AFR case, a correlation between  $\overline{Pr}$  and  $\langle c_{dens} \rangle$  can be guessed.  $f_{dens}$  and  $\langle r_{dens} \rangle$  are more strongly correlated than in the AMA case. At least, they seem to increase continuously together during rainy periods, while  $N_{dens}$  remains very small. This suggests an organized convection regime, in which density currents merge together to form scarce but large structures.
3. In the ATL case, no clear correlation between  $\overline{Pr}$  magnitude and density current statistics can be seen.  $f_{dens}$  and  $\langle r_{dens} \rangle$  are still correlated, but less clearly than in the land cases. Most statistics are pretty much constant during the rainy period. This might suggest a “pop-corn” convection regime, in which density currents, either do not interact with each other, or collide, but as if the whole population was in “equilibrium”, with steady statistics.
4. The BAR case exhibits a very pronounced diurnal cycle of precipitation during this simulation period, as already mentioned by Vial et al. (2019), which seems to exert a strong control on the density current statistics. Here,  $\overline{Pr}$ ,  $N_{dens}$  and  $f_{dens}$  are strongly correlated. In that case, the density current spatial coverage is directly driven by the number of convective cells but individual objects have approximately the same size  $\langle r_{dens} \rangle \sim 7$  km and the same velocity  $\langle c_{dens} \rangle \sim 12$  m s<sup>-1</sup>. This might also be the sign of a scattered (or “pop-corn”) convective regime, in which small individual cells are quasi-homogeneously distributed in space and have approximatively the same life cycle, ending into an equilibrium state even more prominent than in the ATL case.

### 5.2.2. Consistency of the BAR Case at Higher Spatial Resolutions

No parameterization for shallow convection is present in the model setup (see Section 3). Then, we tested the relevance of the detection method in a LES configuration, in the presence of PBL coherent eddies. To do so, we used the ICON model in LES mode over the Barbados region. These simulations (here-after referred to as BAR2 and BAR3) have respectively 300-, and 150-m horizontal grid spacing, and 150 vertical levels (with a layer thickness of about 80 m at 930 m height). The BAR2 domain extends from 60° to 50°W, 11° to 15°N, and the BAR3 domain, from 59.5° to 58°W, 12.6° to 13.6°N. The physical parameterizations for turbulence and microphysics are described in Dipankar et al. (2015) and realistic case simulation results are discussed in Heinze et al. (2017). We consider the simulations run for December 11, 2013. The initialization (at 9:00 UTC, 5:00 LT) and the nudging of the lateral boundaries (every hour) are done via the output of the model described in Section 3. The model is integrated for 27 h.

To detect and count density currents in the output, we applied the density current object identification described in Section 4. Figure 17 shows a map of the density currents detected at 5:30 LT in the two simulations. In the two cases, the method is able to detect gusts, density currents, and their environment. The

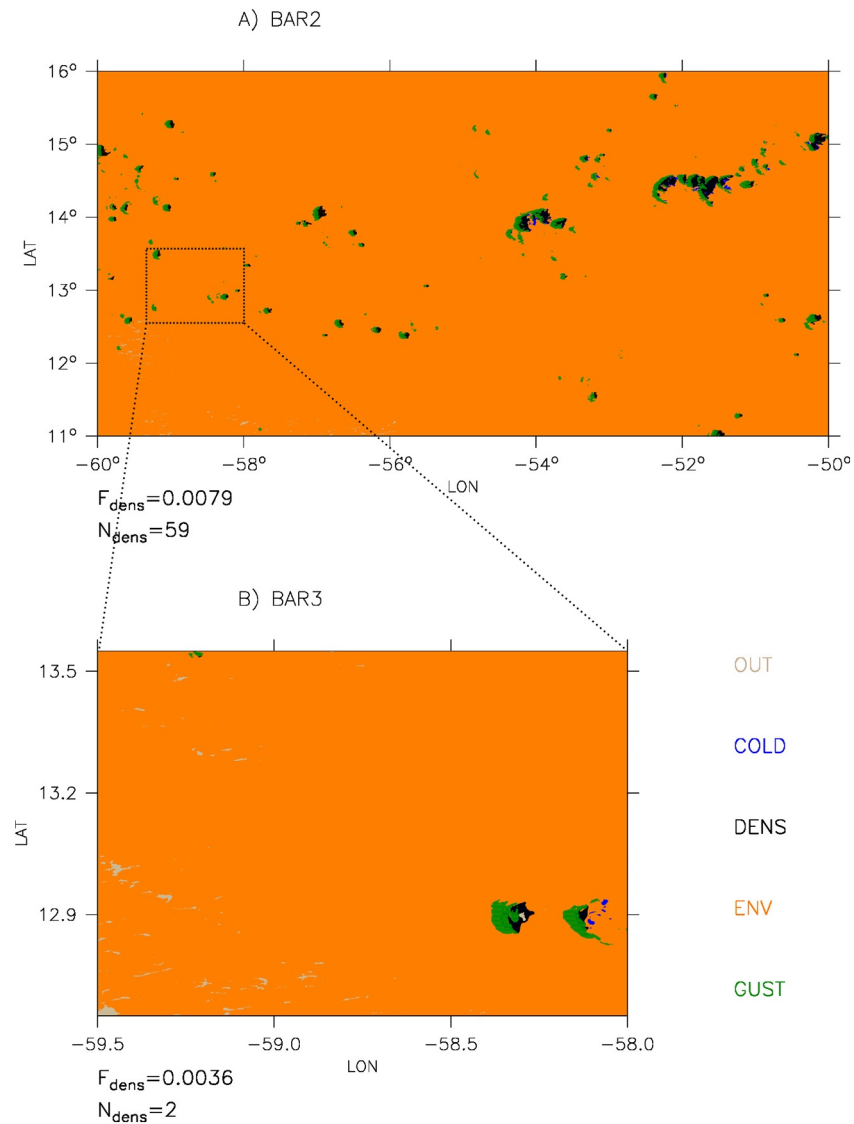


**Figure 17.** Same as Figure 12 for two simulations over the Barbados region with respective horizontal grid-spacings of 300 m for the domain BAR2, and 150 m for the domain BAR3. The dotted rectangle shows which part of the BAR2 domain corresponds to the BAR3 domain. Below the figures, the density current number  $N_{dens}$  and their fractional coverage  $f_{dens}$  are displayed. The cloud scenes simulated in BAR2 and BAR3 have both been taken at 05:30 LT.

introduction of small-scale eddies from diffusive turbulence and nonlocal transport (i.e., thermals) does not seem to induce any adverse effect on the density current detection method presented here.

To check the consistency of these results with the coarser resolution runs of the previous sections, the temporal evolution of density currents' statistics similar to the one presented in Figure 16 are presented in Figure 18 for one simulation day starting at 8 a.m. LT on December 11, 2013. Figure 18a shows that the density currents' number and their fractional coverage follow closely the precipitation signal, as was already the case for the BAR time series displayed in Figure 16 (panel d). The values are also consistent with the ones shown in Figure 16 (panel d). The diurnal cycle observed in these two variables is also consistent with what was found previously over the Barbados region. In the lower panel (b), the signal is less clear, but this can be easily explained by the weak convective activity present into this small subdomain.

While preliminary, these results indicate that the method of density currents' identification exposed in this paper might be relevant for a wide range of resolutions, ranging from hectometer to kilometer simulations.

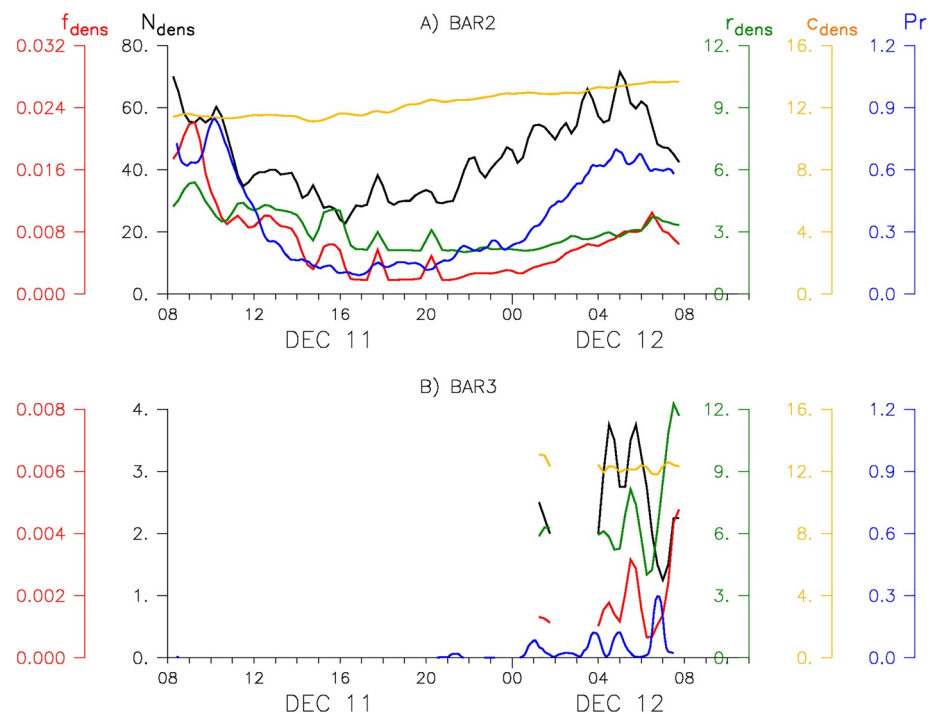


**Figure 18.** Same as Figure 16 but for BAR2 and BAR3 simulations. Time series (local time) are constructed from 15-min snapshots, they are smoothed over a 30-min time window, and cover one simulation day.

Even though this test does not validate the robustness of the method, it already demonstrates its applicability at LES resolution.

## 6. Conclusion

Density currents are key elements for convection internal dynamics and its coupling with the large-scale environment. Starting from a parameterization development perspective, in which a scale separation between density currents and the large-scale flow is required, we designed a new methodology aimed at the detection and the characterization of density currents in convection-permitting models. Contrary to many other studies, this methodology does not make any *a priori* assumption on the spatial scale of the large-scale environment, but instead makes assumptions on the geometrical and physical properties of the subcloud layer anomaly related to the passage of density currents. Consequently, instead of using anomalies defined with regard to a reference large-scale value, the detection method rather discriminates the object from the large-scale, thanks to a reference temperature defined at the interface between these two regions (i.e., in the gust front). By doing so, the method first targets the gust as a buffer area, which blends both properties of the cold pools and their environment. Since the gusts usually cover a small area and are usually clustered in the regions where convection is the most active, they sample the PBL properties solely at locations relevant for density currents. Therefore, even if considering a large study domain of, say  $5^\circ \times 5^\circ$ , and including a sharp SST gradient, convective-free regions (on the cold side of the gradient) will be filtered out (i.e., the OUT region). This makes the present method, in principle, less sensitive to sources of PBL variability other than density currents. As these sources of variability have more chances to be met in large domains, this renders the method also less sensitive to the domain size, up to a certain point.

The method is thought to target the specific imprint of density currents in distinct contexts, in order to capture their track in realistic simulations. This method is also devoided of any tracer and any threshold in precipitation, what represents a significant difference to the vast majority of current algorithms devoted to density current—or cold pool—detection in high-resolution simulations. By revisiting pioneering concepts and recent observational studies, we designed a conceptual picture of density currents based on the key idea that they consist of a core—the cold pool—preceded by a leading edge—the gust front. Thus, density



current detection requires the detection of these two constitutive elements together, contrary to many other methods.

Thanks to this new protocol for detecting density currents, different proxies and properties of density currents could be derived from the analysis of the four snapshots selected from the ICON-NARVAL simulation:

1. In the vertical direction, density currents consist of a turbulent mixed layer in  $\theta_v$  close to the surface, topped by a stratified layer in  $\theta_v$ . Frequently, the stratified layer even includes a temperature inversion.
2. Gust fronts consist of a wind burst combined with a strong temperature gradient, resulting in a local maximum of cooling by horizontal advection in the low levels. The gust combines thermodynamic properties from both cold pools and their close environment, placing them at the interface between those two regions.
3. In the horizontal direction, density currents consist of a “mixed ring” close to their edge, in which turbulence dominates, and a “stratified dome” close to their center, in which the surface turbulent layer is very thin and the stratified layer occupies almost the whole PBL depth. Density currents’ height is overall higher in the stratified dome than in the mixed ring.
4. Our method can extract a key proxy of density currents, namely their height, contrary to most of the other density current detection methods. Our method paves the way to a 3D analysis of density currents in explicit models, most useful to a dynamical study of their interactions with their environment.
5. The density currents detected through this method are not fully correlated in space and time with surface precipitation as they spread around their parent cloud and sustain a while after their initiation by precipitation. In other words, the present method assumes that density currents have their own dynamics, and are not anymore solely a by-product of moist convection.
6. The relative orientation of the gusts with the background wind can change depending on (i) the ambient shear, (ii) the convection stage (i.e., shallow or deep), and (iii) the convective organization (i.e., scattered or aggregated).
7. The number, the fractional coverage, the radius and the velocity of density currents vary a lot in time and from case to case. The combined analysis of these new quantitative proxies provides relevant information on the convection internal dynamics and its interactions with the large-scale flow. A further analysis of these metrics may greatly help constraining convective schemes.
8. The detection method looks consistent in time and across resolutions. It uses two arbitrary parameters and one filtering criterion, which altogether prevent artifacts and, consequently, drastically reduce high frequency noise in time series.

Nevertheless, the present methodology still has some limitations:

1. It cannot be used in too large domains, except maybe if the surface conditions are perfectly homogeneous. The superposition of  $\theta_{v,mix}$  heterogeneities of different scales makes it very difficult to define an homogenous environment of cold pools
2. Its robustness still needs to be assessed (i) over longer timescales, (ii) in regions where breeze circulations are present, and (iii) at different resolutions to quantify its scale awareness.
3. Some improvements could also be made in the detection method, especially to reduce the number of arbitrary thresholds. For instance, one pathway could be to design an iterative method to compute  $\theta_{v,mix}^{ref}$  in a more objective way.
4. The estimate of the height  $h_{top}$  of the density current at a given location is based on a comparison between the local  $\theta_v$  profile with a mean profile in the environment  $\overline{\theta_v^{env}}$ , which tends to underestimate  $\theta_{v, strat}^{ref} = \overline{\theta_{v,mix}^{env}}$ , and then  $h_{top}$ .
5. The hypothesis  $\vec{U}_{mix} \approx \vec{U}_{sfc}$  used to compute advection of  $\theta_v$  by the gust is not physically consistent as the mixed layer inside density currents is supposed to experience a strong wind shear.
6. The method does not follow density currents in time, and thus does not account for splitting/merging processes. Rendering it capable to do that represents a fairly straightforward area for improvement.
7. The code still needs some improvements before being easy to share, in such a way that anyone could use it almost as a “black box”.

In summary, this new methodology offers a real potential for future analyses of the internal dynamic of convection in high-resolution simulations from the perspective of density currents. Although only a short

analysis could be presented here to assess its relevance, it already shows that this methodology can potentially be transposed to any kind of explicit simulation. Here, the 2D-fields and the quantitative proxies derived from our approach provide a lot of information on the thermodynamical, dynamical, geometrical, and statistical properties of density currents, as well as their spatial and temporal evolution. Moreover, in addition to the quantitative proxies analyzed in Section 5, many others (not shown) have been derived like (i) surface fluxes contrast between density currents and their environment, (ii) moisture contrast, (iii) divergence in the mixed layer, (iv) vorticity in the mixed layer, and (v) vertical velocity at the top of the mixed layer. These numerous diagnostics will presumably deserve some attention for understanding the internal dynamics of convection and better constraining existing (or future) convective parameterizations.

The use of convective schemes in GCMs is increasingly questioned as several nonhydrostatic models are now able to perform global simulations (Stevens et al., 2019). For about 20 years, superparameterizations (M. F. Khairoutdinov & Randall, 2001), ultraparameterizations (Parishani et al., 2017) and, more recently, deep-learning approaches (Gentine et al., 2018) have been thought to be promising signs of the near end of the so-called “convective parameterization deadlock” (Randall et al., 2003). However, this study illustrates that parameterizations are powerful guidelines as they ask the question of the scale separation between an object and the large-scale flow in which it is embedded. They provide comprehensive representations, useful to capture coherent structures “hidden” in the turbulent flow. Once identified in convection-permitting simulations, the analysis of these structures—or objects—offers, in turn, new insights and constraints for parameterization development purposes. Hence, the current efforts in exploring new pathways to overcome the parameterization deadlock should not be at the expense of physically based approaches (by opposition to numerically based), which are still very efficient. The transposition of parameterization common constraints such as scale separation, universality, or scale-awareness into the world of high-resolution models is definitively a promising way to break the convective parameterization deadlock.

## Data Availability Statement

Primary data and source codes that were used to generate the results may be obtained from the authors (email: [nicolas.rochetin@lmd.ipsl.fr](mailto:nicolas.rochetin@lmd.ipsl.fr)). After acceptance, they will be archived by the DKRZ (German Climate Computing Center) and available via the specific DOIs <https://doi.org/10.26050/WDCC/Narval1> and <https://doi.org/10.26050/WDCC/Narval2>, generated by the DKRZ technical support, whom the authors also wish to thank for their precious help.

## Acknowledgments

The authors thank the two anonymous reviewers for their numerous and constructive comments. Their meticulous reading greatly helped to improve the quality of the manuscript. The authors warmly thank Daniel Klocke for performing the NARVAL simulations. The authors also thank Caroline Muller, Sandrine Bony, Raphaëla Vogel and Jean-Yves Grandpeix for their insightful comments and inputs, as well as the French Centre National d'Etudes Spatiales (CNES) for funding this publication.

## References

- Baldauf, M., Seifert, A., Förstner, J., Majewski, D., Raschendorfer, M., & Reinhardt, T. (2011). Operational convective-scale numerical weather prediction with the COSMO model: Description and sensitivities. *Monthly Weather Review*, 139(12), 3887–3905. <https://doi.org/10.1175/mwr-d-10-05013.1>
- Berson, F. (1958). Some measurements on undercutting cold air. *Quarterly Journal of the Royal Meteorological Society*, 84(359), 1–16. <https://doi.org/10.1002/qj.49708435902>
- Betts, A. K., & Jakob, C. (2002). Study of diurnal cycle of convective precipitation over Amazonia using a single column model. *Journal of Geophysical Research*, 107(D23), 4732. <https://doi.org/10.1029/2002jd002264>
- Black, P. G. (1978). Mesoscale cloud patterns revealed by Apollo-Soyuz photographs. *Bulletin of the American Meteorological Society*, 59(11), 1409–1419. [https://doi.org/10.1175/1520-0477\(1978\)059<1409:mcprrba>2.0.co;2](https://doi.org/10.1175/1520-0477(1978)059<1409:mcprrba>2.0.co;2)
- Böing, S. J., Jonker, H. J., Siebesma, A. P., & Grabowski, W. W. (2012). Influence of the subcloud layer on the development of a deep convective ensemble. *Journal of the Atmospheric Sciences*, 69(9), 2682–2698. <https://doi.org/10.1175/jas-d-11-0317.1>
- Brient, F., Couvreur, F., Villefranche, N., Rio, C., & Honnert, R. (2019). Object-oriented identification of coherent structures in large eddy simulations: Importance of downdrafts in stratocumulus. *Geophysical Research Letters*, 46(5), 2854–2864. <https://doi.org/10.1029/2018gl081499>
- Browning, K. A., & Ludlam, F. (1962). Airflow in convective storms. *Quarterly Journal of the Royal Meteorological Society*, 88(376), 117–135. <https://doi.org/10.1002/qj.49708837602>
- Canut, G., Couvreur, F., Lothon, M., Pino, D., & Saïd, F. (2012). Observations and large-eddy simulations of entrainment in the sheared sahelian boundary layer. *Boundary-Layer Meteorology*, 142(1), 79–101. <https://doi.org/10.1007/s10546-011-9661-x>
- Charba, J. (1974). Application of gravity current model to analysis of squall-line gust front. *Monthly Weather Review*, 102(2), 140–156. [https://doi.org/10.1175/1520-0493\(1974\)102<0140:aogcmr>2.0.co;2](https://doi.org/10.1175/1520-0493(1974)102<0140:aogcmr>2.0.co;2)
- Colin, M., Sherwood, S., Geoffroy, O., Bony, S., & Fuchs, D. (2019). Identifying the sources of convective memory in cloud-resolving simulations. *Journal of the Atmospheric Sciences*, 76(3), 947–962. <https://doi.org/10.1175/jas-d-18-0036.1>
- Craig, R., & Goff (1976). Vertical structure of thunderstorm outflows. *Monthly Weather Review*, 104(11), 1429–1440. [https://doi.org/10.1175/1520-0493\(1976\)104<1429:vsoto>2.0.co;2](https://doi.org/10.1175/1520-0493(1976)104<1429:vsoto>2.0.co;2)

- de Szoeke, S. P., Skillingstad, E. D., Zuidema, P., & Chandra, A. S. (2017). Cold pools and their influence on the tropical marine boundary layer. *Journal of the Atmospheric Sciences*, 74(4), 1149–1168. <https://doi.org/10.1175/jas-d-16-0264.1>
- Dipankar, A., Stevens, B., Heinze, R., Moseley, C., Zängl, G., Giorgetta, M., & Brdar, S. (2015). Large eddy simulation using the general circulation model ICON. *Journal of Advances in Modeling Earth Systems*, 7(3), 963–986. <https://doi.org/10.1002/2015ms000431>
- Drager, A. J., & van den Heever, S. C. (2017). Characterizing convective cold pools. *Journal of Advances in Modeling Earth Systems*, 9(2), 1091–1115. <https://doi.org/10.1002/2016ms000788>
- Droegemeier, K. K., & Wilhelmson, R. B. (1987). Numerical simulation of thunderstorm outflow dynamics. Part I: Outflow sensitivity experiments and turbulence dynamics. *Journal of the Atmospheric Sciences*, 44(8), 1180–1210. [https://doi.org/10.1175/1520-0469\(1987\)044<1180:nsotod>2.0.co;2](https://doi.org/10.1175/1520-0469(1987)044<1180:nsotod>2.0.co;2)
- Dudhia, J., Moncrieff, M., & So, D. (1987). The two-dimensional dynamics of West African squall lines. *Quarterly Journal of the Royal Meteorological Society*, 113(475), 121–146.
- Emanuel, K. A. (1991). A scheme for representing cumulus convection in large-scale models. *Journal of the Atmospheric Sciences*, 48(21), 2313–2329. [https://doi.org/10.1175/1520-0469\(1991\)048<2313:ASFRCC>2.0.CO;2](https://doi.org/10.1175/1520-0469(1991)048<2313:ASFRCC>2.0.CO;2)
- Enger, N. A., Stensrud, D. J., & Coniglio, M. C. (2008). Surface characteristics of observed cold pools. *Monthly Weather Review*, 136(12), 4839–4849. <https://doi.org/10.1175/2008mwr2528.1>
- Fankhauser, J. (1976). Structure of an evolving hailstorm, Part II: Thermodynamic structure and airflow in the near environment. *Monthly Weather Review*, 104(5), 576–587. [https://doi.org/10.1175/1520-0493\(1976\)104<0576:soaehp>2.0.co;2](https://doi.org/10.1175/1520-0493(1976)104<0576:soaehp>2.0.co;2)
- Feng, Z., Hagos, S., Rowe, A. K., Burleyson, C. D., Martini, M. N., & de Szoeke, S. P. (2015). Mechanisms of convective cloud organization by cold pools over tropical warm ocean during the AMIE/DYNAMO field campaign. *Journal of Advances in Modeling Earth Systems*, 7(2), 357–381. <https://doi.org/10.1002/2014ms000384>
- Fournier, M. B., & Haerter, J. O. (2019). Tracking the gust fronts of convective cold pools. *Journal of Geophysical Research: Atmosphere*, 124(21), 11103–11117. <https://doi.org/10.1029/2019jd030980>
- Gaynor, J., & Ropelewski, C. (1979). Analysis of the convectively modified gate boundary layer using in situ and acoustic sounder data. *Monthly Weather Review*, 107(8), 985–993. [https://doi.org/10.1175/1520-0493\(1979\)107<0985:aotcmg>2.0.co;2](https://doi.org/10.1175/1520-0493(1979)107<0985:aotcmg>2.0.co;2)
- Gentine, P., Garelli, A., Park, S.-B., Nie, J., Torri, G., & Kuang, Z. (2016). Role of surface heat fluxes underneath cold pools. *Geophysical Research Letters*, 43(2), 874–883. <https://doi.org/10.1002/2015gl067262>
- Gentine, P., Pritchard, M., Rasp, S., Reinaudi, G., & Yacalis, G. (2018). Could machine learning break the convection parameterization deadlock? *Geophysical Research Letters*, 45(11), 5742–5751. <https://doi.org/10.1029/2018gl078202>
- Gottschalk, J., Roundy, P. E., Schreck, C. J., III, Vintzileos, A., & Zhang, C. (2013). Large-scale atmospheric and oceanic conditions during the 2011–12 dynamo field campaign. *Monthly Weather Review*, 141(12), 4173–4196. <https://doi.org/10.1175/mwr-d-13-00022.1>
- Grandpeix, J.-Y., & Lafore, J.-P. (2010). A density current parameterization coupled with Emanuel's convection scheme. Part I: The models. *Journal of the Atmospheric Sciences*, 67(4), 881–897. <https://doi.org/10.1175/2009jas3044.1>
- Grandpeix, J.-Y., Lafore, J.-P., & Cheruy, F. (2010). A density current parameterization coupled with Emanuel's convection scheme. Part II: 1D simulations. *Journal of the Atmospheric Sciences*, 67(4), 898–922. <https://doi.org/10.1175/2009jas3045.1>
- Haerter, J. O. (2019). Convective self-aggregation as a cold pool-driven critical phenomenon. *Geophysical Research Letters*, 46(7), 4017–4028. <https://doi.org/10.1029/2018gl081817>
- Heinze, R., Dipankar, A., Henken, C. C., Moseley, C., Sourdeval, O., Trömel, S., et al. (2017). Large-eddy simulations over Germany using ICON: A comprehensive evaluation. *Quarterly Journal of the Royal Meteorological Society*, 143(702), 69–100. <https://doi.org/10.1002/qj.2947>
- Henneberg, O., Meyer, B., & Haerter, J. O. (2020). Particle-based tracking of cold pool gust fronts. *Journal of Advances in Modeling Earth Systems*, 12(5), e2019MS001910. <https://doi.org/10.1029/2019ms001910>
- Hirt, M., Craig, G. C., Schäfer, S. A., Savre, J., & Heinze, R. (2020). Cold pool driven convective initiation: Using causal graph analysis to determine what convection permitting models are missing. *Quarterly Journal of the Royal Meteorological Society*, 146, 2205–2227.
- Hourdin, F., Rio, C., Grandpeix, J.-Y., Madeleine, J.-B., Cheruy, F., Rochetin, N., et al. (2020). LMDZ6A: The atmospheric component of the IPSL climate model with improved and better tuned physics. *Journal of Advances in Modeling Earth Systems*, 12, e2019MS001892. <https://doi.org/10.1029/2019MS001892>
- Jacobsen, M. Z. (2005). *Fundamentals of atmospheric modeling*. Cambridge university press.
- Jeevanjee, N., & Romps, D. M. (2013). Convective self-aggregation, cold pools, and domain size. *Geophysical Research Letters*, 40(5), 994–998. <https://doi.org/10.1002/grl.50204>
- Johnson, R. H., & Nicholls, M. E. (1983). A composite analysis of the boundary layer accompanying a tropical squall line. *Monthly Weather Review*, 111(2), 308–319. [https://doi.org/10.1175/1520-0493\(1983\)111<0308:acaotb>2.0.co;2](https://doi.org/10.1175/1520-0493(1983)111<0308:acaotb>2.0.co;2)
- Khairoutdinov, M. F., & Randall, D. (2006). High-resolution simulation of shallow-to-deep convection transition over land. *Journal of the Atmospheric Sciences*, 63(12), 3421–3436. <https://doi.org/10.1175/jas3810.1>
- Khairoutdinov, M. F., & Randall, D. A. (2001). A cloud resolving model as a cloud parameterization in the NCAR community climate system model: Preliminary results. *Geophysical Research Letters*, 28(18), 3617–3620. <https://doi.org/10.1029/2001gl013552>
- Khairoutdinov, M. F., & Randall, D. A. (2003). Cloud resolving modeling of the arm summer 1997 IOP: Model formulation, results, uncertainties, and sensitivities. *Journal of the Atmospheric Sciences*, 60(4), 607–625. [https://doi.org/10.1175/1520-0469\(2003\)060<0607:crmota>2.0.co;2](https://doi.org/10.1175/1520-0469(2003)060<0607:crmota>2.0.co;2)
- Klemp, J. B., Rotunno, R., & Skamarock, W. C. (1994). On the dynamics of gravity currents in a channel. *Journal of Fluid Mechanics*, 269, 169–198. <https://doi.org/10.1017/s0022112094001527>
- Klocke, D., Brueck, M., Hohenegger, C., & Stevens, B. (2017). Rediscovery of the doldrums in storm-resolving simulations over the tropical Atlantic. *Nature Geoscience*, 10(12), 891–896. <https://doi.org/10.1038/s41561-017-0005-4>
- Knupp, K. (2006). Observational analysis of a gust front to bore to solitary wave transition within an evolving nocturnal boundary layer. *Journal of the Atmospheric Sciences*, 63(8), 2016–2035. <https://doi.org/10.1175/jas3731.1>
- McDonald, J. M., & Weiss, C. C. (2021). Cold pool characteristics of tornadic quasi-linear convective systems and other convective modes observed during vortex-se. *Monthly Weather Review*, 149, 821–840. <https://doi.org/10.1175/MWR-D-20-0226.1>
- Miller, M. (1978). The Hampstead storm: A numerical simulation of a quasi-stationary cumulonimbus system. *Quarterly Journal of the Royal Meteorological Society*, 104(440), 413–427. <https://doi.org/10.1002/qj.49710444014>
- Moncrieff, M. (1978). The dynamical structure of two-dimensional steady convection in constant vertical shear. *Quarterly Journal of the Royal Meteorological Society*, 104(441), 543–567. <https://doi.org/10.1002/qj.49710444102>
- Moncrieff, M. W. (1992). Organized convective systems: Archetypal dynamical models, mass and momentum flux theory, and parametrization. *Quarterly Journal of the Royal Meteorological Society*, 118(507), 819–850. <https://doi.org/10.1002/qj.49711850703>

- Moncrieff, M. W., & Miller, M. J. (1976). The dynamics and simulation of tropical cumulonimbus and squall lines. *Quarterly Journal of the Royal Meteorological Society*, 102(432), 373–394. <https://doi.org/10.1002/qj.49710243208>
- Pantillon, F., Knippertz, P., Marsham, J. H., & Birch, C. E. (2015). A parameterization of convective dust storms for models with mass-flux convection schemes. *Journal of the Atmospheric Sciences*, 72(6), 2545–2561. <https://doi.org/10.1175/jas-d-14-0341.1>
- Parishani, H., Pritchard, M. S., Bretherton, C. S., Wyant, M. C., & Khairoutdinov, M. (2017). Toward low-cloud-permitting cloud superparameterization with explicit boundary layer turbulence. *Journal of Advances in Modeling Earth Systems*, 9(3), 1542–1571. <https://doi.org/10.1002/2017ms000968>
- Park, S. (2014). A unified convection scheme (UNICON). Part I: Formulation. *Journal of the Atmospheric Sciences*, 71(11), 3902–3930. <https://doi.org/10.1175/jas-d-13-0233.1>
- Parker, D. J., & Diop-Kane, M. (2017). *Meteorology of tropical West Africa: The forecasters' handbook*. John Wiley & Sons.
- Provod, M., Marsham, J., Parker, D., & Birch, C. (2016). A characterization of cold pools in the West African Sahel. *Monthly Weather Review*, 144(5), 1923–1934. <https://doi.org/10.1175/mwr-d-15-0023.1>
- Qian, L., Young, G. S., & Frank, W. M. (1998). A convective wake parameterization scheme for use in general circulation models. *Monthly Weather Review*, 126(2), 456–469. [https://doi.org/10.1175/1520-0493\(1998\)126<0456:acwpsf>2.0.co;2](https://doi.org/10.1175/1520-0493(1998)126<0456:acwpsf>2.0.co;2)
- Randall, D., Khairoutdinov, M., Arakawa, A., & Grabowski, W. (2003). Breaking the cloud parameterization deadlock. *Bulletin of the American Meteorological Society*, 84(11), 1547–1564. <https://doi.org/10.1175/bams-84-11-1547>
- Redl, R., Fink, A. H., & Knippertz, P. (2015). An objective detection method for convective cold pool events and its application to northern Africa. *Monthly Weather Review*, 143(12), 5055–5072. <https://doi.org/10.1175/mwr-d-15-0223.1>
- Romps, D. M., & Jeevanjee, N. (2016). On the sizes and lifetimes of cold pools. *Quarterly Journal of the Royal Meteorological Society*, 142(696), 1517–1527. <https://doi.org/10.1002/qj.2754>
- Rotunno, R., Klemp, J. B., & Weisman, M. L. (1988). A theory for strong, long-lived squall lines. *Journal of the Atmospheric Sciences*, 45(3), 463–485. [https://doi.org/10.1175/1520-0469\(1988\)045<0463:atfsl>2.0.co;2](https://doi.org/10.1175/1520-0469(1988)045<0463:atfsl>2.0.co;2)
- Schlemmer, L., & Hohenegger, C. (2014). The formation of wider and deeper clouds as a result of cold-pool dynamics. *Journal of the Atmospheric Sciences*, 71(8), 2842–2858. <https://doi.org/10.1175/jas-d-13-0170.1>
- Seifert, A., & Heus, T. (2013). Large-eddy simulation of organized precipitating trade wind cumulus clouds. *Atmospheric Chemistry and Physics*, 13, 5631–5645. <https://doi.org/10.5194/acp-13-5631-2013>
- Simpson, J. (1969). A comparison between laboratory and atmospheric density currents. *Quarterly Journal of the Royal Meteorological Society*, 95(406), 758–765. <https://doi.org/10.1002/qj.49709540609>
- Simpson, J., & Britter, R. (1980). A laboratory model of an atmospheric mesofront. *Quarterly Journal of the Royal Meteorological Society*, 106(449), 485–500. <https://doi.org/10.1002/qj.49710644907>
- Snodgrass, E. R., Di Girolamo, L., & Rauber, R. M. (2009). Precipitation characteristics of trade wind clouds during RICO derived from radar, satellite, and aircraft measurements. *Journal of Applied Meteorology and Climatology*, 48(3), 464–483. <https://doi.org/10.1175/2008jamc1946.1>
- Stevens, B., Satoh, M., Auger, L., Biercamp, J., Bretherton, C. S., Chen, X., et al. (2019). Dyamond: The dynamics of the atmospheric general circulation modeled on non-hydrostatic domains. *Progress in Earth and Planetary Science*, 6(1), 61. <https://doi.org/10.1186/s40645-019-0304-z>
- Terai, C., & Wood, R. (2013). Aircraft observations of cold pools under marine stratocumulus. *Atmospheric Chemistry and Physics*, 13(19), 9899–9914. <https://doi.org/10.5194/acp-13-9899-2013>
- Thorpe, A., Miller, M., & Moncrieff, M. (1980). Dynamical models of two-dimensional downdraughts. *Quarterly Journal of the Royal Meteorological Society*, 106(449), 463–484. <https://doi.org/10.1002/qj.49710644906>
- Thorpe, A., Miller, M., & Moncrieff, M. (1982). Two-dimensional convection in non-constant shear: A model of mid-latitude squall lines. *Quarterly Journal of the Royal Meteorological Society*, 108(458), 739–762. <https://doi.org/10.1002/qj.49710845802>
- Thorpe, A. J., & Miller, M. J. (1978). Numerical simulations showing the role of the downdraught in cumulonimbus motion and splitting. *Quarterly Journal of the Royal Meteorological Society*, 104(442), 873–893. <https://doi.org/10.1002/qj.49710444203>
- Torri, G., & Kuang, Z. (2016). Rain evaporation and moist patches in tropical boundary layers. *Geophysical Research Letters*, 43(18), 9895–9902. <https://doi.org/10.1002/2016gl070893>
- Torri, G., & Kuang, Z. (2019). On cold pool collisions in tropical boundary layers. *Geophysical Research Letters*, 46(1), 399–407. <https://doi.org/10.1029/2018gl080501>
- Torri, G., Kuang, Z., & Tian, Y. (2015). Mechanisms for convection triggering by cold pools. *Geophysical Research Letters*, 42(6), 1943–1950. <https://doi.org/10.1002/2015gl063227>
- Vial, J., Vogel, R., Bony, S., Stevens, B., Winker, D. M., Cai, X., et al. (2019). A new look at the daily cycle of trade wind cumuli. *Journal of Advances in Modeling Earth Systems*, 11(10), 3148–3166. <https://doi.org/10.1029/2019ms001746>
- Vogel, R., Konow, H., Schulz, H., & Zuidema, P. (2021). A climatology of trade-wind cumulus cold pools and their link to mesoscale cloud organization. *Submitted to Atmospheric-Chemistry and Physics*. <https://doi.org/10.5194/acp-2021-420>
- Vogel, R., Nuijens, L., & Stevens, B. (2016). The role of precipitation and spatial organization in the response of trade-wind clouds to warming. *Journal of Advances in Modeling Earth Systems*, 8(2), 843–862. <https://doi.org/10.1002/2015ms000568>
- Wakimoto, R. M. (1982). The life cycle of thunderstorm gust fronts as viewed with Doppler radar and Rawinsonde data. *Monthly Weather Review*, 110(8), 1060–1082. [https://doi.org/10.1175/1520-0493\(1982\)110<1060:tlcotg>2.0.co;2](https://doi.org/10.1175/1520-0493(1982)110<1060:tlcotg>2.0.co;2)
- Warner, C., Simpson, J., Helvoirt, G. V., Martin, D., Suchman, D., & Austin, G. (1980). Deep convection on day 261 of gate. *Monthly Weather Review*, 108(2), 169–194. [https://doi.org/10.1175/1520-0493\(1980\)108<0169:dcodog>2.0.co;2](https://doi.org/10.1175/1520-0493(1980)108<0169:dcodog>2.0.co;2)
- Weaver, J. F., & Nelson, S. P. (1982). Multiscale aspects of thunderstorm gust fronts and their effects on subsequent storm development. *Monthly Weather Review*, 110(7), 707–718. [https://doi.org/10.1175/1520-0493\(1982\)110<0707:maotgf>2.0.co;2](https://doi.org/10.1175/1520-0493(1982)110<0707:maotgf>2.0.co;2)
- Zängl, G., Reinert, D., Ripodas, P., & Baldauf, M. (2015). The ICON (ICOsahedral Non-hydrostatic) modelling framework of DWD and MPI-M: Description of the non-hydrostatic dynamical core. *Quarterly Journal of the Royal Meteorological Society*, 141(687), 563–579. <https://doi.org/10.1002/qj.2378>
- Zipser, E. (1977). Mesoscale and convective-scale downdrafts as distinct components of squall-line structure. *Monthly Weather Review*, 105(12), 1568–1589. [https://doi.org/10.1175/1520-0493\(1977\)105<1568:macdad>2.0.co;2](https://doi.org/10.1175/1520-0493(1977)105<1568:macdad>2.0.co;2)
- Zuidema, P., Torri, G., Muller, C., & Chandra, A. (2017). A survey of precipitation-induced atmospheric cold pools over oceans and their interactions with the larger-scale environment. *Surveys in Geophysics*, 38(6), 1283–1305. <https://doi.org/10.1007/s10712-017-9447-x>